Journal of Volcanology and Geothermal Research 481 (2027) 108751

Contents lists available at ScienceDirect

Journal of Volcanology and Geothermal Research

journal homepage: www.journals.elsevier.com/journal-of-volcanology-and-geothermal-research

The 2019 pumice raft and submarine eruption of Volcano F, Tofua-Kermadec Arc, from field spectroscopy, remote sensing and machine learning

Alice M. Hopkins [a,*], Susanna K. Ebmeier [a], Timothy J. Craig [a], Isobel A. Yeo [b]

[a] COMET, School of Earth, Environment and Sustainability, University of Leeds, Leeds, LS2 9JT, UK
[b] National Oceanography Centre Southampton, European Way, Southampton, SO14 3ZH, UK

ARTICLE INFO

Keywords:
Ocean remote sensing
Machine learning
Field spectroscopy
Submarine volcanism
Pumice rafts
Ocean discolouration

ABSTRACT

The eruption of submarine volcanoes is a poorly-characterised source of marine hazard, largely due to the difficulty of observing such eruptions. Pumice rafts are a potentially-hazardous product of submarine volcanic eruptions: they pose danger to shipping, wildlife and impact livelihoods of those living in small island nations. However, our understanding of pumice rafts is limited due to rafting events often going unnoticed and occurring in remote areas. In this study, we analyse the pumice raft produced in the 2019 eruption of Volcano F in the Tonga Arc, southwest Pacific. We demonstrate that raft evolution, including waterlogging, can be detected using remote sensing methods, by identifying diagnostic spectral characteristics associated with saturated pumice. Using field spectroscopy, we observe unique spectral signatures in pumice samples, from this eruption and other eruptive settings, and compare these to the satellite-derived spectral measurements of the raft. We additionally show that pumice spectra are distinct from spectra of other floating debris.

These spectral signatures can be used to identify pumice from samples and remotely using satellites. Using pumice samples from the 2019 raft, collected at various distances from the vent of Volcano F, we show that samples that spent longer at sea are more eroded although their circularity remains similar regardless of collection location. We show that with increased time at sea, the raft thickness decreases, whilst its saturation and uniformity increase. Our study demonstrates that, beyond capturing the presence of pumice, spectral satellite analysis can be linked to pumice raft physical properties.

We detect two previously unreported eruptive periods at Volcano F, Tofua-Kermadec Arc, using a combination of satellite remote sensing and machine learning analysis of discoloured seawater. Additionally, we use the same methods to detect and observe submarine volcanic activity at Home Reef, Tofua-Kermadec Arc.

Plain Language Summary In this paper, we use a mixture of satellite imagery and sample analysis to learn more about submarine volcanic processes at two volcanoes: Volcano F and Home Reef. We can observe periods of submarine volcanic activity using satellites by looking for pumice rafts, changes in ocean colour and volcanic plumes in the atmosphere. Pumice is a type of rock that is produced during explosive eruptions and forms into a raft which can float on the ocean. In our study, we analyse spectral properties of pumice samples from the 2019 Volcano F eruption and compare them to satellite images of the pumice raft to determine how saturated the raft is. We study how the size and shapes of the rock samples change with distance from volcano. We use machine learning to scan through satellite images for 25 years at Volcano F and Home Reef for potential eruptions. We detect three previously known eruptive periods–two at Volcano F and one at Home Reef and then two new periods of discoloured seawater at Volcano F.

1. Introduction

1.1. Submarine Volcanism and remote sensing

It is thought that around three-quarters of the volcanoes on Earth are found underwater (Siebert et al., 2011), but submarine volcanoes are relatively understudied as they are remote, logistically challenging and costly to access and, due to the overlying water cover, problematic for most near-field or remote monitoring techniques. As a result, they are usually poorly or totally unmonitored. Thus, satellite remote sensing, while limited to those processes occurring either at the surface or at

* Corresponding author.
E-mail addresses: eeah@leeds.ac.uk (A.M. Hopkins), S.K.Ebmeier@leeds.ac.uk (S.K. Ebmeier), T.J.Craig@leeds.ac.uk (T.J. Craig), i.yeo@noc.ac.uk (I.A. Yeo).

https://doi.org/10.1016/j.jvolgeores.2026.108751
Received 16 June 2026; Received in revised form 24 September 2026; Accepted 28 September 2026
Available online 13 October 2026
0377-0273/Crown Copyright © 2026 Published by Elsevier B.V. This is an open access article under the CC BY license (http://creativecommons.org/licenses/by/4.0/).

shallow depths, is in many cases the only tool available for identifying and reconstructing volcanic activity in the oceans (Mantas et al., 2011; Eugenio et al., 2014; Jutzeler et al., 2020).

Explosive submarine eruptions can create a signal at the sea surface detectable by satellite (Brandl et al., 2020; Yeo et al., 2024; Manga et al., 2018; Jutzeler et al., 2014). These signals typically occur when the eruptive vent is shallow enough for gas expansion to overcome hydrostatic pressure, which was thought to be limited to vents < 500 metres deep (Colombier et al., 2025). The 2012 eruption of Havre Seamount, Southwest Pacific 897 metres below sea level, was the first documented eruption to show that deeper vents can erupt explosively to generate a signal at the sea surface (Jutzeler et al., 2014). Most submarine volcanoes exist on mid-ocean ridges and can erupt explosively but are too deep for any signals to be detected at the sea surface (Helo et al., 2011).

Previous studies have used remote sensing data for the observation and analysis of a variety of submarine eruptive products observable on or above the sea surface, such as pumice rafts (see Section 1.2), discoloured seawater and subaerial eruptive plumes (e.g., Zheng et al., 2022; He et al., 2025; Brandl et al., 2020; Chen et al., 2022; Bryan et al., 2012; Yeo et al., 2024; Urai and Machida, 2005; Mantas et al., 2011).

Submarine volcanic activity, either eruptive or related to degassing, can change the ocean colour due to the release of chemicals and the promotion of phytoplankton blooms (Urai and Machida, 2005; Urai, 2014; Ciancia et al., 2026). Seawater discolouration is either formed directly by the release of volcanic material into the ocean or as a secondary effect from the release of iron-rich volcanic materials into the ocean causing phytoplankton blooms to form (Mantas et al., 2011). Chemicals released (e.g., SiO_2, Al_2O_3 and Fe_2O_3) into the ocean change the ocean colour, with a range of colour changes from milky white to reddish-brown (higher Fe_2O_3 concentration) and even yellow-green (higher Fe and Al concentration) (Urai and Machida, 2005). Phytoplankton growth is typically limited by the availability of iron (Fe) in the high-nitrate low-chlorophyll regions of the oceans (Boyd et al., 2007), and the release of Fe from volcanic ash is thought to create the optimum ocean conditions for phytoplankton blooms (Browning et al., 2014). Other chemical species released during eruptions such as Cu, Si, P and NH_4^+ potentially also produce a similar phytoplankton response (Mackey et al., 2002; Olgun et al., 2008). Phytoplankton blooms have a distinctive spectral signature due to the presence of chlorophyll-a (Klemas, 2010), which causes absorption peaks at blue and red wavelengths (~440–470 nm and ~665 nm, respectively), a reflectance peak in the green (~560 nm) and an increased reflection in red-edge wavelengths (~705 nm) compared with the absorption at red wavelengths (Kangro et al., 2026; Brewin et al., 2019). Where phytoplankton is present in Sentinel-2 and Moderate Resolution Imaging Spectroradiometer (MODIS) imagery we would therefore expect high reflectance in the green band and increased absorption in the blue band, compared with surrounding background ocean, and expect strong absorption in red and blue bands. In Sentinel-2 imagery, phytoplankton blooms would also cause a large increase in reflectance in the red edge band, compared with absorption in the red band as chlorophyll absorbs light at red wavelengths but scatters light in the red edge wavelengths (Kangro et al., 2026).

Subaerial plumes produced by submarine eruptions are predominantly composed of water vapour and ash (Cronin, 1971; Colombier et al., 2025). They can contain smaller volumes of SO_2 than those produced by subaerial eruptions, shown in the 2022 eruption of Hunga Volcano where 93% of the sulfur budget is thought to have entered the ocean during submarine magma fragmentation, instead of being released in the subaerial plume (Wu et al., 2025). Subaerial plumes can occasionally be observed during an eruption if satellite remote sensed imagery happens to be collected during a co-eruptive phase, for example in 2022 at Hunga Volcano (Proud et al., 2022) and in 2020 at Kilauea (Cahalan and Dufek, 2021).

The launch of high resolution satellites with open access data, such as Sentinel-2 in 2015 (Drusch et al., 2012), has resulted in significant improvements to the potential of remote sensing approaches to detect submarine volcanic activity. Combining Sentinel-2 imagery, with high spatial resolution (10 m optical pixels) but a 5-day repeat time with imagery from NASA's MODIS satellite (lower spatial resolution (500 m optical) but more frequent (daily) repeat times (Justice et al., 2002) allows good coverage of submarine eruptive events. The higher spatial resolution of Sentinel-2 images leads to the detection of smaller-scale submarine signals on the ocean surface, whereas with the higher temporal resolution of MODIS we can study larger-scale signals on a daily basis.

1.2. Pumice rafts

Pumice is a highly vesicular porous rock formed by the fragmentation and cooling of siliceous magma in water (Chen et al., 2022; Jutzeler et al., 2016), produced during both explosive subaerial and submarine eruptions (Kano, 2003). In oceanic settings, groups of low-density pumice clasts can coalesce, forming buoyant rafts with sizes up to 200 square km, (Houghton and Wilson, 1989). These rafts can float for years and travel vast distances, depending on surface winds and ocean surface currents (Brandl et al., 2020; Jutzeler et al., 2014; Bryan et al., 2012; Manga et al., 2018; Takeuchi et al., 2024a; Mitchell et al., 2021).

The formation, buoyancy and life cycle of pumice rafts are poorly understood (Bryan et al., 2012). They can form during different types of eruptions, both subaerial and submarine, including submarine explosive eruptions (Takeuchi et al., 2024b), submarine effusive eruptions (Manga et al., 2018), from subaerial pyroclastic density currents entering the sea, (Jutzeler et al., 2014), and from subaerial volcanic plumes falling into seawater (Bryan et al., 2012; Zheng et al., 2022), amongst other processes.

The buoyancy of a raft depends on the pumice density, porosity (both connected and isolated) and permeability (Chen et al., 2022; Takeuchi et al., 2024b). Analogue experiments have shown that initial buoyancy is strongly dependent on the temperature at which the raft is formed (Whitham and Sparks, 1986), which leads to different structures of vesicles within the clasts. At formation temperatures < 150 °C, the hot air inside the pumice contracts, drawing water into the vesicles causing the raft to sink. At hotter temperatures, water inside the vesicles evaporates forcing the air out of the pumice. Upon cooling, this steam condenses and water is re-absorbed. Pumice rafts sink when the pumice becomes saturated. Pumice samples from the 2012 eruption of Havre volcano (Mitchell et al., 2021) show that micro-textural differences between pumices can determine whether pumice floats and forms rafts or sinks to the seafloor post eruption. Takeuchi et al. (2024b) demonstrate the importance of isolated compared with connected porosity in pumice samples. Using pumice from the 2021 eruption of Fukutoku-Oka-no-Ba, they show that particles with a higher isolated porosity, and a lower connected porosity, are unsinkable even on a millimetre particle scale. While it had been thought floating pumice could only be produced at shallow water depths, the 2012 eruption of Havre showed that raft-forming is possible from deep submarine conditions depending on the vesicularity of the erupted pumice. Further, Pegler and Ferguson (2021) show that to match observations of seafloor tephra dispersal, deep (> 500 m depth), explosive eruptions require a large energy flux, driven by high temperatures, suggesting that temperatures required for pumice raft formation are more commonplace than previously thought. Thus, pumice rafts are a common product of marine volcanic eruptions under a variety of conditions, yet are more poorly understood than other hazardous volcanic phenomena.

Pumice rafts have many impacts on the socioeconomics of small island nations, marine traffic and local ecosystems (e.g., Whiteside et al., 2021; Bryan et al., 2012). It is thought that pumice rafts act as a mechanism for carrying marine life, other biological matter and

volcanic material across the oceans, to sites far from the source volcano (Ohno et al., 2022; Elser et al., 2015). They can also prevent sunlight entering the ocean for the duration of their float time, curtailing the extent of the neritic zone and endangering local wildlife. Lastly, they impact on atmospheric-oceanic heat and gas interactions (Jutzeler et al., 2020). The impacts on humans can be significant: for shipping near volcanic arcs, pumice rafts pose a danger of critical damage to water intakes and engine cooling systems, and lead to route diversions resulting in economic losses (Brandl et al., 2020). Pumice rafts often wash up on the shores of islands, causing major disruption to vital industries including fishing and tourism, as well as being an obstacle to dock and harbour operations. The 2021 eruption of Fukutoku-Oka-no-Ba produced a pumice raft with a high proportion of millimetre sized particles, which were pulled into cooling systems of vessels and ingested by fish, leading to large amounts of fish deaths (Ohno et al., 2022; Takeuchi et al., 2024b; Akiyama et al., 2022; Tome, 2021). Pumice strands in the ocean can also re-form into secondary rafts during storms (Yoshida K., 2022). Impacts can be delayed or persistent — rafts can float for a long time before they wash up onshore. The raft from the 2012 Havre eruption drifted for several months and was visible from satellite imagery for just over 5 months, with some clasts still afloat up to a year post eruption (Manga et al., 2018; Jutzeler et al., 2014). It is therefore vital that pumice raft detection and monitoring methods improve to enable us to better understand the hazard posed and mitigate their impacts. There remain large gaps in our understanding of pumice rafts including how the remotely-sensed signature of pumice differs between different rafting events, or how that signature evolves during raft ageing. To develop effective monitoring approaches therefore requires the characterisation of raft development during the course of an eruption in terms of both raft physical properties and remote sensing signatures.

One such pumice-raft forming eruption is the 2019 eruption of Volcano F, 18.33°S, 174.37°W - see Section 1.3, which produced both submarine and subaerial eruption plumes, and a substantial pumice raft (Jutzeler et al., 2020; Yeo et al., 2024; Brandl et al., 2020), though the eruption itself went undetected at the time.

Recent studies using Sentinel-2 and machine learning to study pumice rafts include (He et al., 2025) who characterise key properties, such as daily areal coverage, of 8 reported pumice raft events. Our work uses similar remote sensing techniques to He et al. (2025) but additionally links remotely sensed properties to physical sample analysis. Zheng et al. (2022) use supervised machine learning methods to detect previously unreported pumice rafts from the Rabaul caldera region, Papua New Guinea.

1.3. Volcano F

Volcano 0403-091, also known as Volcano F and listed as unnamed volcano number 243091 in the Smithsonian database (Global Volcanism Program, 2024), is a submarine volcano located at 18.33°S, 174.37°W in the Tonga-Kermadec Arc, Kingdom of Tonga, NW of Vava'u, shown in Fig. 1. The Tonga-Kermadec Arc is a subduction zone formed due to the Pacific Plate subducting under the Australian Plate and is one of the most volcanically active island arcs on Earth (Yeo et al., 2024; Global Volcanism Program, 2024). The subsection of the Tonga-Kermadec Arc where Volcano F is located (the Tofua Arc), comprises 14 known volcanoes, and has had 12 recorded submarine eruptions since 2000 (Global Volcanism Program, 2024). Most of these eruptions were Volcanic Explosivity Index (VEI) 3 or less (Global Volcanism Program, 2024), however these volcanoes can produce more explosive eruptions. Most recently, the January 2022 eruption of Hunga Tonga–Hunga Ha'apai Volcano produced the highest eruptive plume ever recorded and was the most explosive eruption this century with a VEI of 5-6 (Borrero et al., 2023; Proud et al., 2022). Volcanism in the Tofua Arc often produces pumice rafts (Bryan et al., 2004) – of the 20 raft-forming eruptions that have taken place at minimum globally over the last 200 years, 9 occurred in the Tofua-Kermadec Arc (Bryan et al., 2012). The closest volcanoes to Volcano F are Fonualei, Late, Home Reef and Lateiki, described in Table 1 and shown on Fig. 1.

Volcano F is a 4 km wide by 7 km long ellipsoidal caldera, with multiple caldera nested floors and is surrounded by radial bedforms, formed by volcaniclastic density flows (Pope et al., 2018). The first bathymetric survey of Volcano F was conducted by the RV Southern Surveyor (expedition SS2004/11 'NoToVE') in 2004. It has had two recorded eruptions, both pumice-forming, in 2001 (VEI 2) and 2019 (VEI 3) (Brandl et al., 2020). The 2001 eruption was detected by the French Polynesian Seismic Network due to the detection of T-wave signals and from pumice clasts collected onshore (Global Volcanism Program, 2024; Bryan et al., 2004). The raft from the 2001 eruption passed through Fiji around 2 months post-eruption (Bryan et al., 2004).

The 2019 eruption was well covered by satellite imagery (Brandl et al., 2020), and the pumice clasts themselves were sampled by NERC researchers at locations where they were beached after differing float times (Yeo et al., 2024). Thus, this is an ideal case study to understand the satellite remote sensing signatures of pumice raft evolution. Volcano F erupted during the period of 6-8th August 2019. The exact eruption date is unknown, but an image captured by Sentinel-2 appears to show two concentric rings at 18.307°S, 174.395°W on the 6th August. These have been hypothesised to be underwater eruption columns (Jutzeler et al., 2020; Brandl et al., 2020), suggesting an eruption start date of 6th August 2019. This eruption released a pumice raft around 200 km^2 detected by MODIS, Sentinel-2 and Landsat-9, amongst other satellites (Brandl et al., 2020). The pumice raft was the longest continuously observable eruptive signal from this eruption, floating for more than eight months. Subaerial and submarine plumes also occurred as part of the eruption but dispersed in under one and two weeks, respectively (Yeo et al., 2024; Brandl et al., 2020). The raft floated westwards, with clasts washing up on islands from the Lau Island group around three weeks after eruption, the Yasawa Islands around six weeks after the eruption and eventually beaching in Eastern Australia in April-May 2020, eight months after the initial eruption (Jutzeler et al., 2020). The raft progression over time, tracked using MODIS and Sentinel-2 imagery, is shown in Fig. 1. Brandl et al. (2020) track the 2019 erupted pumice raft using Sentinel-2 imagery and combine this with seismic data from nearby seismic stations on Niue Island and Rarotonga showing that a series of earthquakes occurred prior to the volcanic eruption.

Volcano F's caldera morphology suggests that it is capable of much larger eruptions (Yeo et al., 2024). The eruptions of 2001 and 2019 may therefore form part of a the caldera cycle, and understanding the role they play in the evolution of the volcano and its magmatic system is fundamental to understanding the hazard posed from larger eruptions (de Maisonneuve et al., 2021). We have chosen Volcano F for this study, due to the excellent available coverage from satellite imagery of the pumice raft and submarine and subaerial plumes, alongside the availability of a unique sample set including samples taken at the eruption site, and sampled from the raft beachings having floated for different periods. The unique set of samples available at Volcano F allows for physical calibration of remotely sensed data.

In this study, we track and analyse the evolution of the 2019 Volcano F pumice raft using MODIS and Sentinel-2 imagery. We compare spectral properties of the pumice clasts under different conditions, measured using field spectroscopy, and link them with spectral properties of the raft itself, measured by satellite imagery. We present a combined field and satellite spectral analysis of pumice samples from an explosively submarine erupted raft to understand how the raft changes with age and saturation. We compare our measured field spectroscopy data with field spectroscopy measurements from other floating debris. We analyse physical changes in pumice clasts from the 2019 Volcano F raft focusing on clast circularity and area. We then develop a machine learning algorithm to run on 25 years of satellite imagery (25 years of MODIS, 7 years of Sentinel-2) at Volcano F and nearby volcano Home Reef to produce a comprehensive eruptive history, including previously undocumented events, of these two volcanoes.

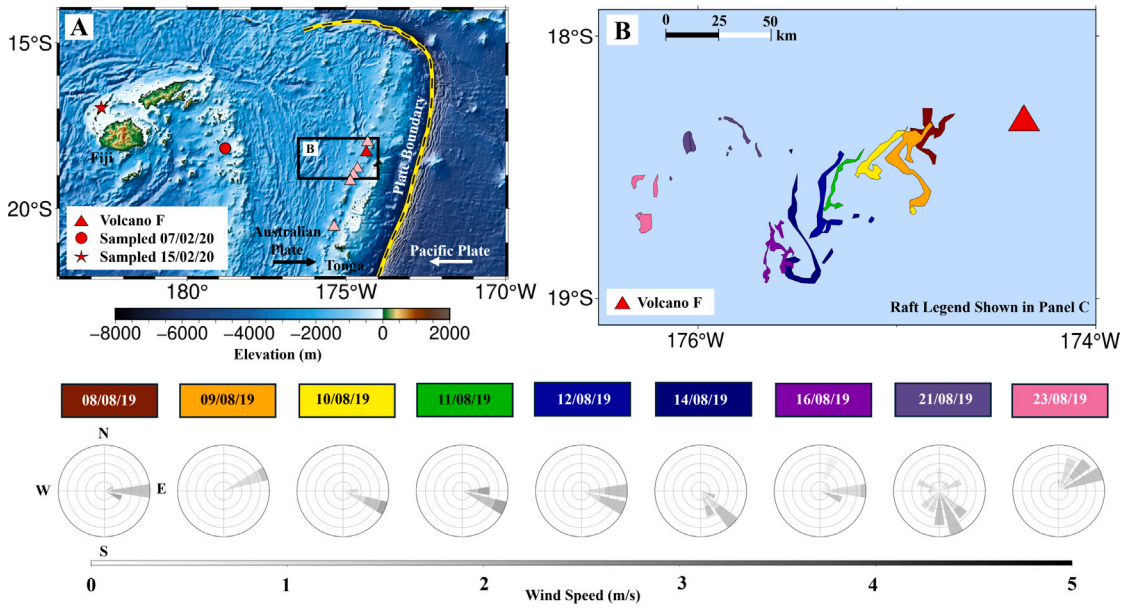


Fig. 1. (a) A bathymetric map showing Volcano F (in red) and the pumice clast sampling locations. In pink, the closest volcanoes to Volcano F are shown (N-S): Fonualei, Late Island, Home Reef, Lateiki and Hunga Tonga–Hunga Ha'apai Volcano. The plate boundary of the Australian and Pacific Plates are shown as a yellow and black line. (b) A map of the pumice raft progression from Volcano F's August 2019 eruption tracked using MODIS Imagery. (c) The wind speed and direction at the sea surface corresponding to each day of the tracked raft in (b).

Table 1
Nearby volcanoes to Volcano F.

Volcano	Distance from Volcano F (km)	Elevation (m)	Most recent eruption	Notes
Fonualei	34	188	1957	Steam venting August 2000
Late	61	565	1854	Steam rising 29/11/2022
Home Reef	81	−10	Ongoing since 2019	Island forming. 2006 eruption produced pumice raft
Lateiki	109	43	Ongoing since 2019	Island forming

2. Data

2.1. Field observations and hand specimens

2.1.1. Pumice samples

Volcano F pumice hand samples, from Lakeba and the Yasawa Islands in Fiji, were collected and petrologically analysed by Yeo et al. (2024). The raft arrived at Lakeba and the Yasawa Islands on the 3rd and 27th September 2019, respectively. They sampled pumice at two locations per beach in a 30 x 30 cm areas above the high-tide level to minimise wave-based erosion. The samples were collected from 7-12th Feb 2020 on Lakeba and 15-16th Feb 2020 from Yasawa, approximately 6 months post eruption. In this study we analyse samples taken from Lakeba Guest House and Waci Waci beach, on Lakeba (three weeks float time), and from Navotua in the Yasawa Islands (six weeks float time). We also analyse Volcano F pumice samples from Cylinder Beach, Australia (eight months float time). Lakeba Island, Yasawa Islands and Cylinder Beach, Australia, are located at 465, 880 and 3443 km from the vent, respectively.

We compare the Volcano F pumice clasts to a range of pumice hand samples measured from different subaerial and submarine eruptive settings, capturing a range of pumice petrologies to assess how representative the spectral properties of the Volcano F pumice are (see Tables 2 and 3).

2.1.2. External field spectroscopy data sources

We use a hyperspectral-reflectance dataset of marine plastic litter samples measured by Knaeps et al. (2020). From this dataset, we use the mean spectral reflectance data from dry wood 1 and dry blue plastic bag (samples sourced from the Port of Antwerp) and from the wet plastic bag (sample not sourced from the marine environment). Additionally, we use data from the USGS Spectral Library Version 7 (Kokaly et al., 2017). We use spectral measurements of Deepwater Horizon emulsified oil with an oil-to-water ratio of 40:60, for layers of 0.1 mm and 8 mm thickness. We choose these specific oil samples as they have a realistic oil-to-water ratio for oil spill patches (Fingas and Fieldhouse, 2004). Our chosen layer thicknesses represent oil slick (< 0.1 mm) and oil mousse (8 mm) scenarios (Fingas, 2021). The plastic litter measurements were made using two instruments: ASD FieldSpec 4 and SEV SR-3501 hyperspectral radiometers. We use the ASD FieldSpec measurements from the USGS spectral library.

2.2. Satellite imagery

We use optical and Short Wave Infrared (SWIR) data from the Moderate Resolution Imaging Spectroradiometer (MODIS) (MOD09GA.061 Terra Surface Reflectance Daily Global 500 m (Vermote and Wolfe, 2015)) and Sentinel-2 (Harmonised Sentinel-2 MSI: MultiSpectral Instrument, Level-2A product (European Union/ESA/Copernicus, 2025)) accessed through Google Earth Engine (GEE hereafter; Gorelick et al., 2017), (see Table 4). MODIS has 36 spatial bands covering 400–1400 nm, with spatial resolutions of 250 m (Bands 1 and 2), 500 m (Bands 3 - 7), 1000 m (Bands 8–36) and a repeat time of 1 day. The Sentinel-2 optical bands and SWIR bands have a 10 and 20 metre spatial resolution, respectively. The repeat time of Sentinel-2 is 5 days and it has 12 spectral bands covering 433–2280 nm, shown in Fig. 2. We analyse MODIS data from 24/02/2000 to 31/12/2025. Throughout those years, we analyse MODIS pumice spectral data

Table 2
Volcano F pumice sampling locations.

Location	Latitude	Longitude	Distance from Vent/km
Lakeba Guest House, Lakeba	−18.23°N	−178.81°E	465
Waci Waci, Lakeba	−18.24°N	−178.78°E	465
Navotua, Yasawa	−16.86°N	177.44°E	880
Cylinder Beach, Australia	−27.42°N	153.53°E	3443

Table 3
Other pumices analysed.

Sample	Composition/SiO_2 (%)	Eruption Year	Environment	Notes	Reference
Havre	Rhyolitic (70%–73%)	2012	Submarine	White	Manga et al. (2018)
Kolumbo	Rhyolitic (73.7%–74.2%)	1650	Submarine	White; Bio weathering	Vougioukalakis et al. et al. (2025)
Volcano F	Dacitic (63%–70%)	2019	Submarine	Grey	Yeo et al. (2024)
Holuhraun	Basaltic (47.5%–48.5%)	2014	Subaerial	Dark black	Halldórsson et al. (2018)
Las Canadas	Unknown	Unknown	Subaerial	Reddish-brown	
Melimoyu	Rhyodacite (70%)	2850 BP	Subaerial	Yellow	Geoffroy et al. (2018)
Mt Hekla	Andesitic–Dacitic (54%–64%)	1947	Subaerial	White	Geist et al. (2021)

Table 4
The spatial, temporal and spectral characteristics of satellite data used to characterise and detect eruptive sequences in this study.

	Spatial resolution	Repeat time	Bands
Sentinel-2	10 m (Optical), 20 m (SWIR)	5 days	13 Spectral Bands (433–2280 nm)
MODIS	250 m (Bands 1–2) 500 m (Bands 3–7) 1000 m (Bands 8–36)	1 day	36 Spectral Bands (400–14,400 nm)

from 27/09/2001 to 12/10/2001, between 08/08/2006 - 21/08/2006 and between 08/08/2019 and 16/08/2019. Once developed, we run our algorithm on Sentinel-2 Level-2A data between 01/12/2018 and 31/12/2025. We analyse Sentinel-2 Level-2A pumice spectral data between 08/08/2019 and 16/08/2019.

2.3. Additional geophysical datasets

We use ERA5 Single Levels reanalysis from the Copernicus Climate Data Store (CDS) in Fig. 1 analysing data between 08/08/2019 and 23/08/2019 (Hersbach et al., 2020).

3. Methods

3.1. Spectral pumice sample properties from field spectroscopy

3.1.1. Field spectroscopy measurements

We measure the spectral characteristics of the pumice hand samples to directly compare them with satellite images of the pumice raft. By comparing spectral data from wet, dipped and dry pumice hand samples with satellite data, we can infer whether parts of the raft are saturated. The spectroradiometer used in this study is a SVC HR-1024i Field Spectrometer, measuring wavelengths over the range 350–2500 nm, from visible to short wave infrared light across the electromagnetic spectrum (Spectra Vista Corporation, 2013). Sentinel-2 and MODIS measure over spectral ranges of 443–2190 nm and 405–2155 nm, respectively, leading to a significant overlap in spectral ranges between the measurements taken with the spectrometer and data from satellite imagery used in our study, shown in Fig. 2.

We measure the reflectances under stable lighting conditions in a dark room, with the SVC HR-1024i Field Spectrometer calibrated against a white Spectralon reflectance panel of known spectral reflectance in between measurements. We take the measurements with a lamp and a contact probe set-up, with a contact surface of $\sim 12\,cm^2$ on each sample. From each sampling location, we take 25 measurements, across 5 different clasts. We measure each sample area in 3 different conditions: dry, after submersion in synthetic salt water (35 g/L) for 5 s and after saturation in synthetic salt water for more than 12 h, which we term ‘dry’, ‘dipped’ and ‘wet’, respectively. We did not directly quantify saturation, but treat this duration as a method to produce waterlogged clasts rather than a measured saturation state. We measure every area every 5 s for a period of 150 s and then average over that period. We place an optical cloth underneath each sample to reduce stray lighting effects. Additionally, we measure the reflectances of pumice samples from other eruptions, both subaerial and submarine, to compare with the Volcano F pumice samples.

3.1.2. Convolution of field spectroscopy measurements

We evaluate how field spectroscopy measurements would be observed by Sentinel-2 by convolving our hyperspectral data with the Sentinel-2 spectral response function. For a given band b, the band-integrated reflectance is calculated as:

$$R_{S2,\,b} = \frac{\int_{\lambda_{\min,b}}^{\lambda_{\max,b}} R(\lambda)\, S_b(\lambda)\, d\lambda}{\int_{\lambda_{\min,b}}^{\lambda_{\max,b}} S_b(\lambda)\, d\lambda}$$

where λ is wavelength, $R(\lambda)$ is the hyperspectral reflectance, and $S_b(\lambda)$ is the Sentinel–2 spectral response function (Drusch et al., 2012; Clark, 1999).

3.2. Spectral raft properties from satellite imagery

The satellite images we compare to hand sample data are 3 Sentinel-2 images taken on 11/08/19, 16/08/19 and 21/08/19. The Sentinel-2 images of the raft after these dates are fragmented, and we exclude these from our comparison. Given we do not observe significant spectral variation in the Volcano F pumice samples from different locations which spent differing amounts of time at sea (see Section 4.1), we assume that the time period between satellite acquisition (August 2019) and sample collection (February 2020) does not affect our interpretation. The clasts forming the raft are significantly smaller than the spatial resolution of Sentinel-2 so any holes/edges of clasts are effectively averaged within each pixel.

3.3. Physical pumice sample properties

We measure the physical properties of the pumice samples from the 2019 Volcano F pumice raft collected from different locations to investigate the relationship between the physical properties and time spent at sea. Samples were collected by previous fieldwork on Lakeba and Yasawa Islands. Lakeba Island and Yasawa Islands are located at 465 and 880 km, respectively, from the vent. In this study, images are taken of the pumice samples from each location. We use ImageJ (Schneider et al., 2012) to measure the perimeter and area of each clast. From this, we calculate the circularity, described by Cox (1927):

$$\text{Circularity} = \frac{4\pi \cdot (\text{area})}{(\text{perimeter})^2}$$

3.4. Automated eruption detection

We use two random forest supervised machine learning approaches trained on different datasets for the automatic detection of pumice rafts and discoloured seawater in a test area of 47000 km^2 surrounding Volcano F. The first approach is trained on MODIS imagery — using QGIS (Rosas-Chavoya et al., 2022) we manually labelled 77 MODIS images from 11 different submarine volcanic settings with known eruptions (Volcano F, Home Reef, Ahyi, South Sarigan, Nishinoshima, El Hierro, Fukutoku-Oka-No-ba, Lateiki, Epi-B, Hunga Volcano and Kavachi) with a mixture of eruptive and non-eruptive scenes. For our other random forest algorithm, trained on Level-2 A Sentinel-2 imagery, we labelled 94 Sentinel-2 tiles from the same 11 volcanic settings, again including eruptive and non-eruptive scenes. We labelled images by drawing polygons around objects of 6 different classes and then assigning 2000 points per class, avoiding labelling the same pixel twice. The classes were defined as: (1) pumice, (2) discoloured seawater, (3) cloud, (4) background ocean, (5) land, and (6) subaerial plume. We labelled the images viewing them in Red-Green-Blue and the ratios Red-Green and NIR-Red to ensure that no subtle signals were overlooked in the visible bands. For Sentinel-2, we trained our algorithm on bands 1–12 and the ratios Red-Green and NIR-Red. For MODIS, we trained our algorithm on bands 1–7 and the same ratios as in Sentinel-2. We chose to classify clouds as a separate class rather than use a cloud mask as using cloud masks often masked the signals we were looking for, especially when the signals were partially covered by cloud. Further, the edge of clouds can appear spectrally similar in Red-Green-Blue to pumice rafts. A summary of our labelled datasets is provided in the supplementary materials.

Random forest algorithms use bootstrapping combined with feature randomness to generate uncorrelated, random decision trees (Liu et al., 2012). For classification, every tree predicts the classification of pixels and the majority prediction is taken. We chose to use random forest algorithms due to their effectiveness for large datasets. The ability of a random forest to have multiple trees reduces the likelihood of over-fitting. Further, random forest algorithms are one of the built-in machine learning algorithms in GEE, hence making it easier to scale up to search for previously-undetected submarine eruptions and pumice rafts.

We evaluate the accuracy of our random forest algorithms by computing the training and validation accuracies. We split the data randomly and train our random forest algorithm on 80% of the data from our dataset, saving 20% of the dataset for validation. Our MODIS training dataset contains 135915 samples, and validation dataset contains 34085 samples. Our Sentinel-2 training dataset contains 349640 samples, and validation dataset contains 87410 samples.

We run both trained classifiers on all MODIS/Sentinel-2 images in the area $[-175.5°E, -173.5°E, -19.4°N, -17.4°N]$ from 24/02/2000 to 31/12/2025 for the MODIS imagery and between 01/12/2018 and 31/12/25 for the Sentinel-2 imagery. We use both our algorithms to detect patches of discoloured seawater greater than 100 connected pixels and patches of pumice greater than 50 connected pixels for both and output the classified area of each. We choose > 100 connected pixels for discoloured seawater to exclude small false positives and ensure that only plume-scale features were analysed. For pumice, we used a > 50-pixel threshold, reflecting the typically smaller, more compact morphology of pumice clusters while still removing isolated false positives, which emerge when individual pixels are on the boundaries of features such as clouds. For the MODIS imagery, our minimum possible detection areas are 3.125 km^2 and 6.25 km^2 for pumice and discoloured seawater, respectively. For the Sentinel-2 imagery, our minimum possible detection areas are 0.005 km^2 and 0.01 km^2 for pumice and discoloured seawater, respectively.

3.5. Spectral properties of discoloured seawater

We analyse the spectral signatures of all the discoloured seawater areas detected by our algorithm to determine the sources. We measure the average band values for the areas detected by our algorithm and compare that to areas of background ocean in our image. For both Sentinel-2 and MODIS, we analyse blue, green, red and NIR bands. Additionally for Sentinel-2 we analyse the red edge band. We were unable to analyse chlorophyll-a specifically for the 2001 eruption due to MODIS Aqua not being launched at the time of eruption and the spatial resolution of MODIS Aqua is too coarse to analyse our detected 2020 and 2022 periods of discoloured seawater at Volcano F.

4. Results

4.1. Spectral pumice sample properties from field spectroscopy

4.1.1. Volcano F samples

We find that the spectral properties of all Volcano F samples are very consistent, with the only major differences relating to the water saturation of each sample. Figs. 2a, b and c show the spectral reflectance signatures of Volcano F pumice samples under three saturation conditions: dry, dipped and wet. The reflectance curve has local maxima close to 725 and 1600 nm and a local minimum around 1050 nm present in all the Volcano F samples, regardless of pumice saturation. The dipped and wet pumice samples have additional minima around 1400, 1900 and 2500 nm, which are not present in the dry sample spectral reflectance values. The dipped and wet pumice samples are less reflective than the dry samples and the pumice gets visibly darker when it is more saturated. The minima due to pumice saturation are mostly in areas of the electromagnetic spectrum not covered by Sentinel-2 bands. However, the continuous increase in reflectance across higher wavelength values in the dry samples (a decrease for the dipped and wet samples) overlaps slightly with Sentinel-2's Short Wave InfraRed bands B11 and B12. The spectral properties of the hand samples are consistent within 0.03 units of absolute spectral reflectance across all collection locations

4.1.2. Pumice samples from other eruptions

Comparing the field spectroscopy measurements of Volcano F pumice to samples from other geographically-disparate eruptions reveals distinct spectral differences, with variations in reflectance and curve shape linked to eruption history, composition, and alteration state. Fig. 2d compares the field spectroscopy measurements of the different submarine pumice hand samples. The Havre and Volcano F samples follow the similar distinctive shape with a local maxima around 725 nm. The pumice from Havre has a higher reflectance than that from Volcano F, shown in the visible bands by its white colour, compared with the grey of the Volcano F samples. The eruptive sample from Kolumbo has a higher reflectance across the spectrum than those of the Havre and Volcano F samples and the shape of the curve is quite different. The Kolumbo eruptive sample shows evidence of biological weathering. Fig. 2e shows the field spectroscopy measurements of subaerial pumice hand samples. All the samples except for the Holuhraun sample have the distinctive local maxima around 725 nm. The Melimoyu and Mt Hekla sample follow similar curves for the rest of the spectrum. The Holuhraun sample has very low reflectivity.

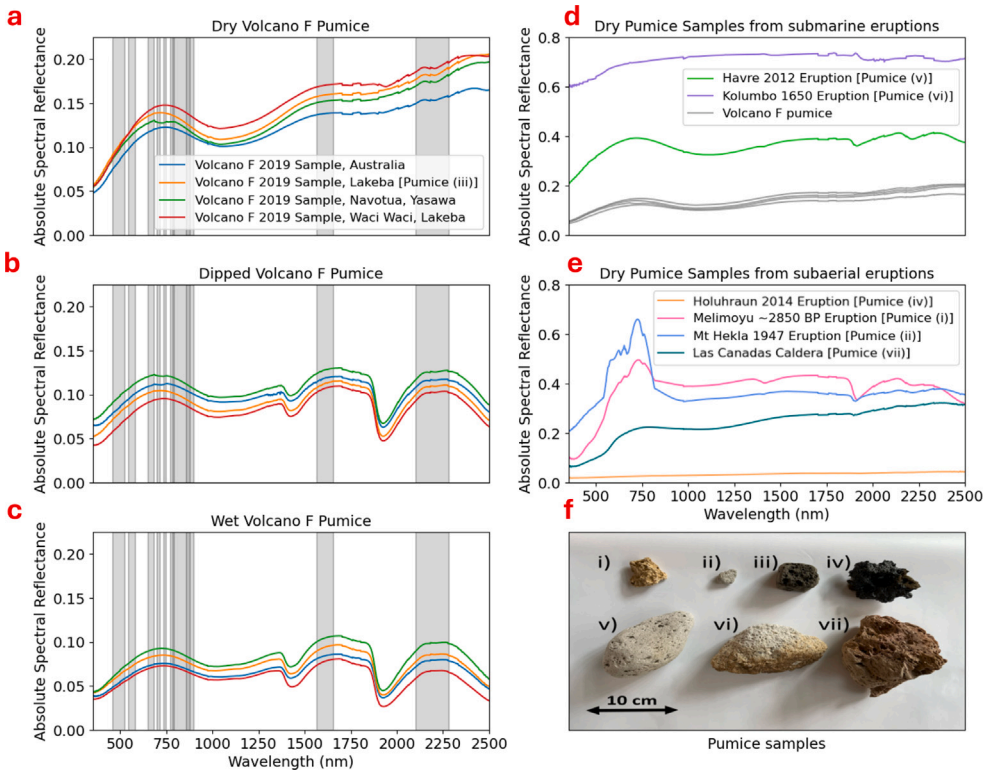


Fig. 2. (a), (b) and (c) show the spectral reflectance of Volcano F pumice samples measured dry, dipped and wet with field spectroscopy. These are overlaid on top of the Sentinel-2 bands. (d) and (e) show the spectral reflectance of dry pumice samples produced by submarine and subaerial eruptions, respectively. The pumice image shows all the pumice samples used to make the above figures. The pumices in (f) are from the following eruptions: (i) Melimoyu 2850 BP, (ii) Mt Hekla 1947, (iii) Volcano F 2019, (iv) Holuhraun 2014, (v) Havre 2012, (vi) Kolumbo 1650, (vii) Las Canadas Caldera.

4.1.3. Comparison of pumice with other types of floating debris

We compare the spectral reflectance of our Volcano F pumice samples with other types of floating debris using both the field spectroscopy measurements and their Sentinel-2–convolved spectra, showing that pumice exhibits a distinctive reflectance curve in both.

Fig. 3A shows the comparison between our Volcano F pumice field spectroscopy measurements and data from other floating debris. Both oil samples display minima around 375 nm, leading to wide maxima between 750 and 1400 nm. They have additional minima at 1400, 1900 and 2500 nm. The 8 mm thick layer of oil has higher overall maxima than the 0.1 mm thick layer and displays an additional local minimum at 1200 nm. Both plastic bag samples display similarly shaped curves — with maxima at 475 nm, between 700 and 1300 nm and at 1800 nm and minima around 360, 1400, 1900 and 2500 nm. The dry driftwood has a wide maxima between 600 and 1350 nm. It has minima at 1400, 1900 and 2500 nm. The Volcano F pumice spectra are described in 4.1.1.

Fig. 3B shows the hyperspectral data from Fig. 3A as if it were observed by Sentinel-2. The dry Volcano F pumice shows an increase from Bands 1–4, fairly constant reflectance from bands 4–8A, with a dip in reflectance for Band 9 and an increase from Bands 9–12. The dipped and wet Volcano F pumices follow the same shape as the dry pumice, although are less reflective generally, and then display a dip from Band 11 to 12. The oil samples both follow the same shape with a sharp increase in reflectance from Bands 1–9 and then a decrease from Bands 9–12. The 8 mm thick oil layer shows larger increases and decreases compared with the 0.1 mm thick layer. The dry plastic bag has an increase in reflectance from Bands 1–2 followed by a sharp decrease for Bands 2–5. The reflectance increases again for Bands 5–9 and then decreases between Bands 9 and 12. The wet plastic bag decreases between Bands 1–4, is steady between Bands 5–8, decreases from Bands 9–11 and increases at Band 12. The dry driftwood reflectance increases from Band 1 until Band 10, where it decreases until Band 12.

4.2. Physical sample properties

Volcano F pumice samples that were collected from an island closer to the eruptive vent in general are larger and less spherical than samples collected further away, shown in Fig. 4. 9631 samples were collected from Yasawa (850 km from vent) and 4734 from Lakeba (465 km from vent). We analyse the areas of the pumice clasts showing that the samples collected from Lakeba (closer to vent) on average have a higher area compared with those from Yasawa. The samples from Yasawa show a higher measure of circularity across the distributions, suggesting that the pumice samples become more rounded over time through physical inter-clast interaction. The mean circularity values of the samples from Yasawa and Lakeba are 0.706 and 0.654, respectively. The mode circularity values from Yasawa and Lakeba are 0.710 and 0.743. The circularity values for Lakeba samples have a slightly higher standard deviation at 0.144 compared with 0.129 for that of the Yasawa samples.

4.3. Spectral raft properties from satellite imagery

Fig. 5 shows an increase in SWIR reflectance values and a decrease in the Red-Green-Blue reflectance values across towards the centre of the raft. The reflectance values in all bands decrease over time. There were no substantial differences in pumice colour present in the collected samples hence we are confident in attributing colour changes in the raft to waterlogging and raft thickness.

In Fig. 5, we analyse transects across pumice rafts to assess evidence of variations in raft thickness and saturation. We draw transects on Sentinel-2 images of the Volcano F Pumice from 11/08/19, 16/08/19 and 21/08/19, (3–5, 8–10 and 13–15 days post eruption, respectively). There are higher reflectance values in the visible bands towards the edges of the raft, remaining at a lower, constant value across the middle

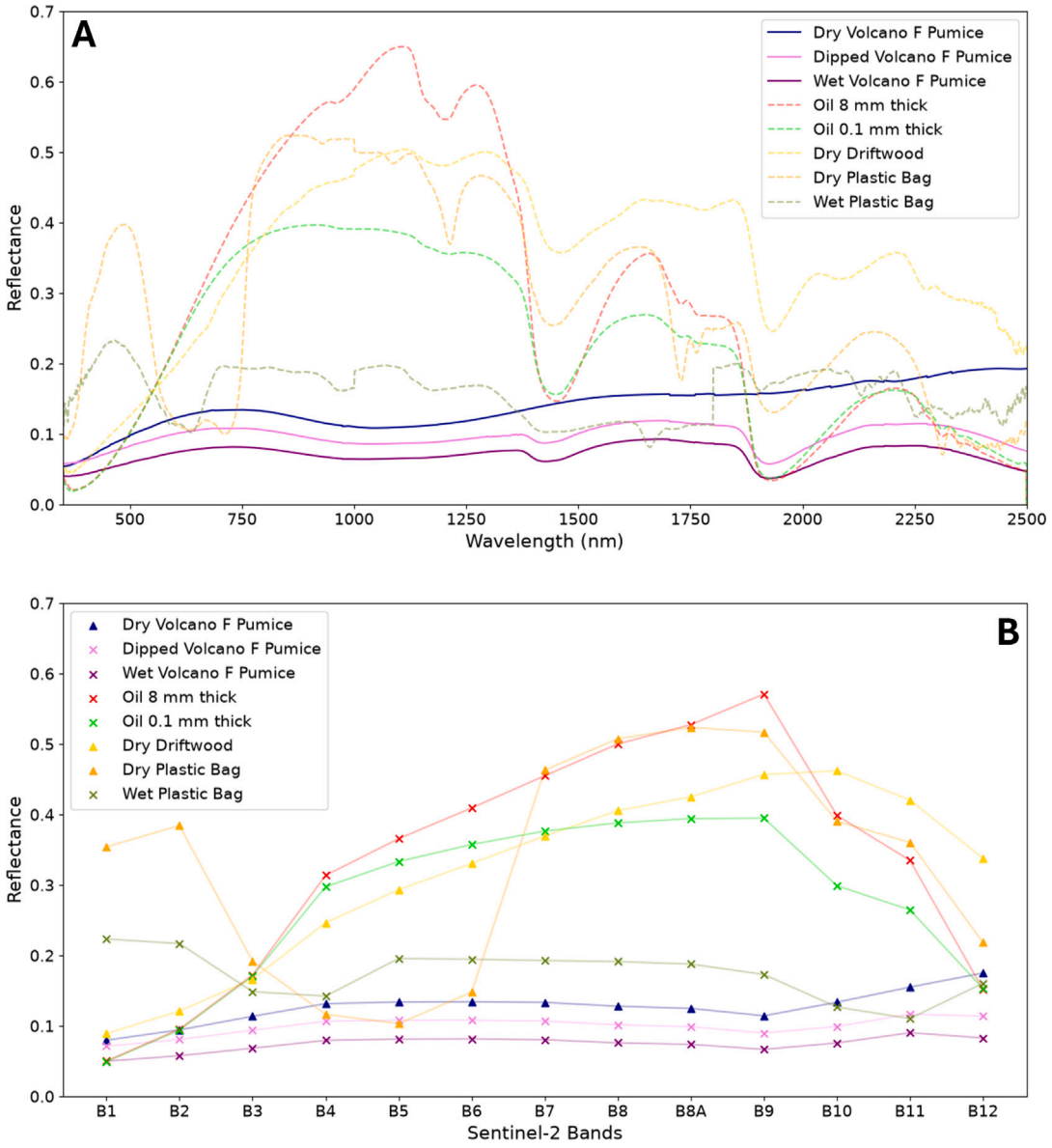


Fig. 3. (A) shows hyperspectral field spectroscopy data of dry, dipped and wet Volcano F pumices compared with plastics, oil and driftwood. (B) shows the hyperspectral data from (A) as if it were observed by Sentinel-2. The crosses correspond to wet samples and triangles to dry samples. Volcano F spectroscopy data measured in this study. Dry driftwood, dry and wet plastic bag spectroscopy data from Knaeps et al. (2020). Oil spectroscopy data from Kokaly et al. (2017).

of the raft, in Transects AA', BB', CC' and DD'. The reflectance values increase in the SWIR bands towards the centre of the raft, and are lower at the edges in Transects AA', BB', CC' and DD'. These effects are not present in Transects EE', FF' and GG' from the final image we analyse (13 – 15 days post eruption). There is also a decrease in reflectance magnitudes with time across the images — the transects across earlier images have on average higher reflectance values than the final image. There are spikes in reflectance values due to cloud and also some lower values due to cloud shadows.

4.4. Supervised machine learning: Random forest

Over our study period, in MODIS imagery we detect three pumice raft-forming eruptions: the September 2001 and August 2019 eruptions of Volcano F (Brandl et al., 2020) and the August 2006 eruption of Home Reef (Bryan et al., 2012). From Sentinel-2 imagery, we again detect the August 2019 Volcano F eruption and then detect two previously unreported episodes of discoloured seawater at Volcano F between June-August 2020 and in July 2022. We also detect frequent volcanic discoloured seawater at Home Reef throughout the Sentinel-2 imagery period. All the above results are shown in Figs. 6, 7, and 8 and summarised in Tables 5, 6, 7, and 8. In our tables, we write 'n/a' where there is no signal observed due to cloud cover in the image or there being no image available. For the MODIS random forest algorithm, we measure our training accuracy to be 0.965 and validation accuracy to be 0.814. For the Sentinel-2 random forest algorithm, we measure our training accuracy to be 0.992 and validation accuracy to be 0.957.

During both the 2006 Home Reef and Volcano F 2001 raft forming eruptions, we detect two distinct areas of seawater discolouration per eruption: green discoloured seawater above the volcanic vents (Type-I Plume) and blue discoloured seawater close to the pumice rafts (Type-II Plume). Plume types follow the morphological classification of Mantas et al. (2011), who report Type-I and Type-II plumes during the 2006 Home Reef eruption. The Volcano F plumes exhibit similar morphological and spectral characteristics, and therefore we adopt the same terminology. However, we note that there may be differences in the species present.

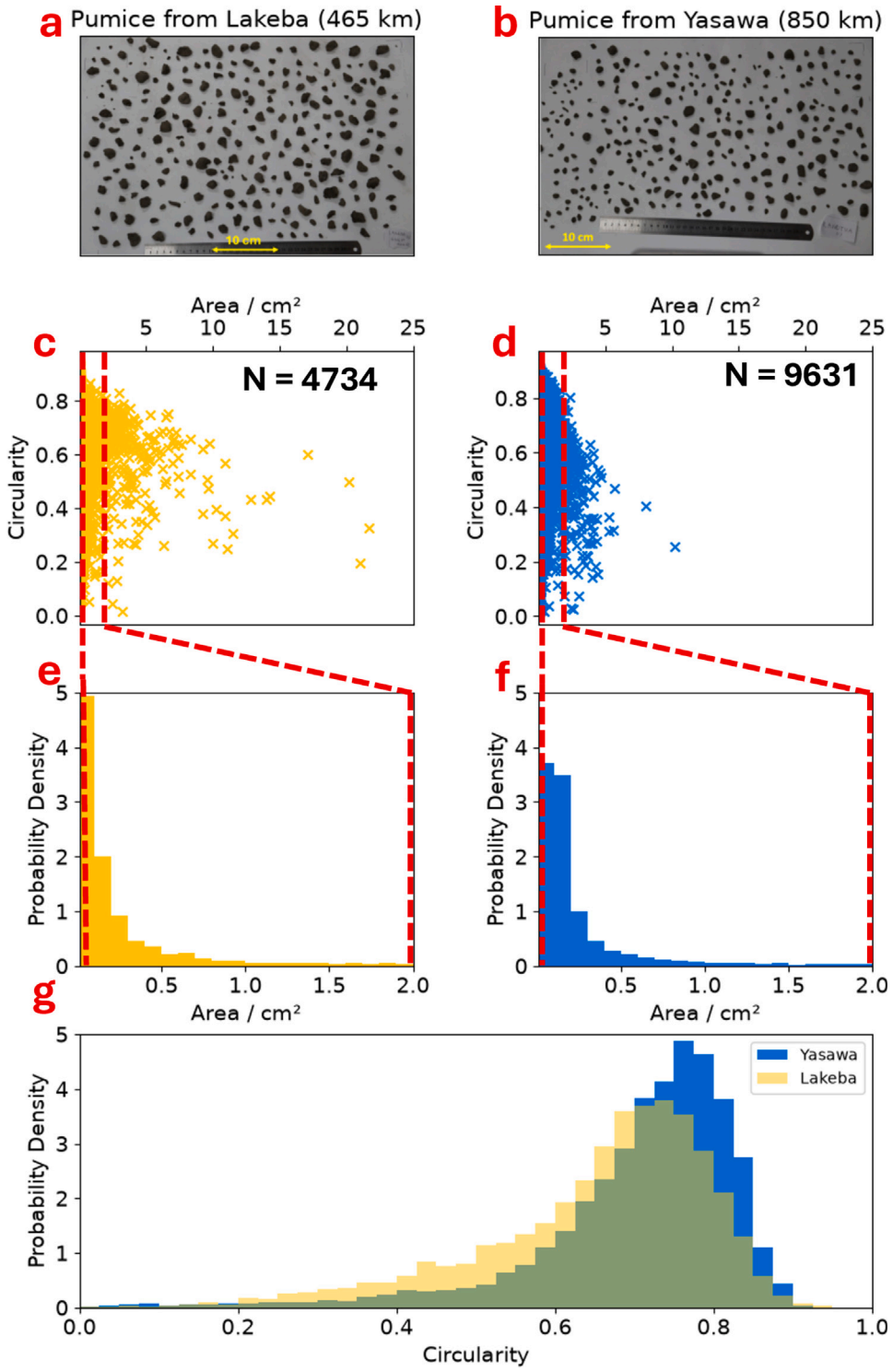


Fig. 4. (a) and (b) show images of pumice hand samples taken from Yasawa (850 km from vent) and Lakeba (465 km from vent). (c) and (d) show the circularity against area of the clasts from Yasawa and Lakeba, respectively. (e) and (f) show the normalised area distributions in the high-density region at < 2 cm squared across the samples collected from Yasawa and Lakeba, respectively. (g) shows the distribution of circularity across the samples.

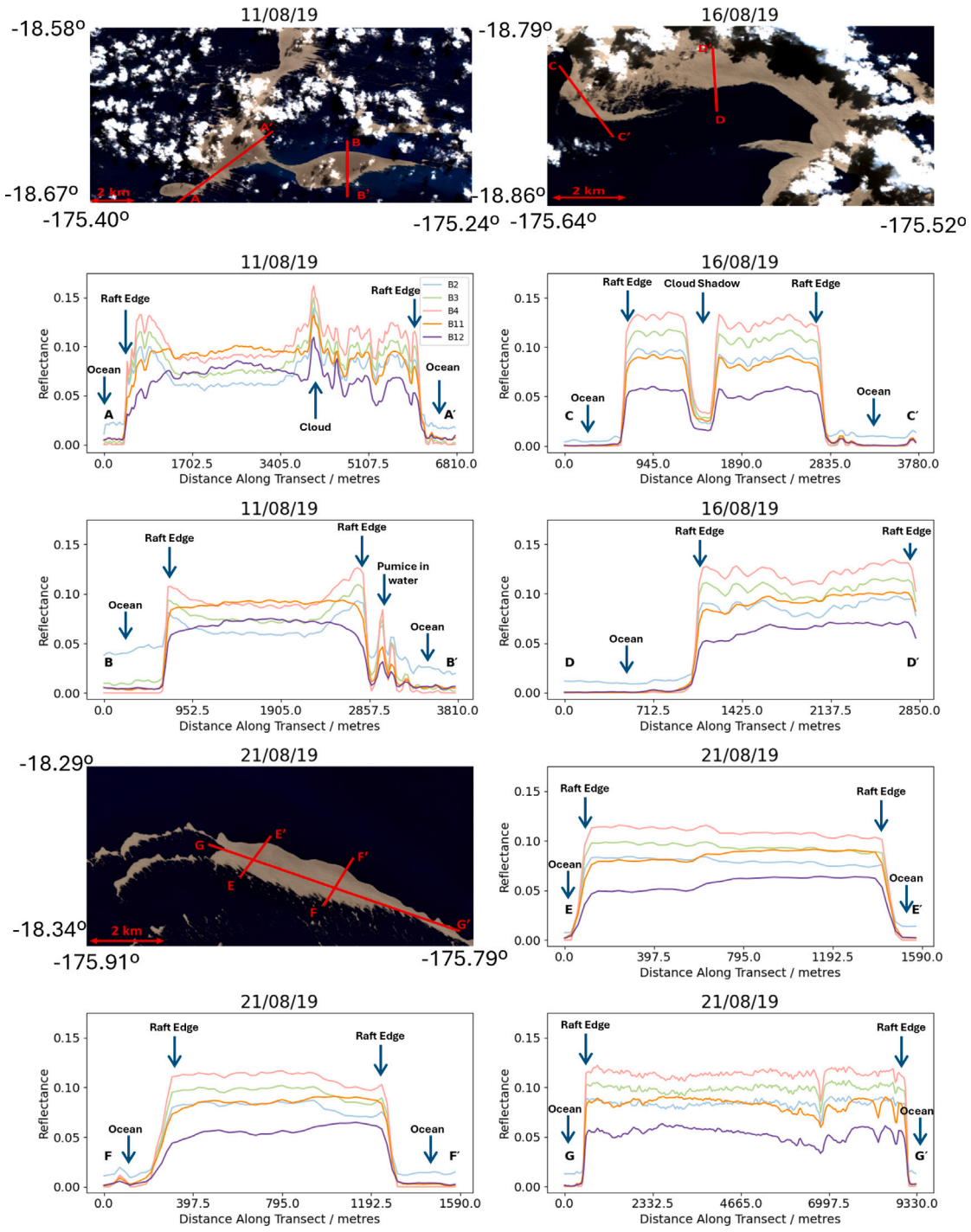


Fig. 5. Spectral reflectances at points along transects of Sentinel-2 images of the Volcano F Pumice from 11/08/19, 16/08/19 and 21/08/19. We create 30 *x* 30 metre tiles along each transect and then calculate average reflectance for each tile for the B2 (Blue), B3 (Green), B4 (Red), B11 and B12 (SWIR) bands. RGB Sentinel-2 images are displayed, showing the transects over each image.

Table 5
Detected areas and descriptions of discoloured seawater and pumice during the Volcano F 2001 eruption.

Date	Discoloured water (km^2)	Pumice (km^2)	Notes	Satellite
27/09/2001	n/a	21.68	None visible – cloudy	MODIS
28/09/2001	n/a	n/a	None visible – cloudy	MODIS
29/09/2001	n/a	n/a	None visible – cloudy	MODIS
30/09/2001	n/a	n/a	None visible – cloudy	MODIS
01/10/2001	271.64	0	Type-I and II Plumes present	MODIS
02/10/2001	n/a	n/a	None visible – cloudy	MODIS
03/10/2001	n/a	n/a	None visible – cloudy	MODIS
04/10/2001	n/a	n/a	None visible – cloudy	MODIS
05/10/2001	472.00	0	Type-I Plume more spread out, rounded. No further observations of Type-II Plume.	MODIS
06/10/2001	420.42	0	Type-I Plume: brighter green above vent	MODIS
07/10/2001	n/a	n/a	No Image	MODIS
08/10/2001	47.85	0	Type-I Plume: Bright green more spread out	MODIS
09/10/2001	n/a	n/a	No Image	MODIS
10/10/2001	361.81	0	Type-I Plume: Faded green	MODIS
11/10/2001	n/a	n/a	None visible – cloudy	MODIS
12/10/2001	47.60	0	Type-I Plume: Faded green	MODIS

Table 6
Detected areas and descriptions of discoloured seawater and pumice during the Volcano F 2019 eruption.

Date	Discoloured water (km^2)	Pumice (km^2)	Notes	Satellite
08/08/2019	327.72	185.66	Type-II Plume: Round, near raft	MODIS
09/08/2019	660.43	196.38	Type-II Plume: More spread out, near raft	MODIS
10/08/2019	794.26	99.69	Type-II Plume: More spread out, brighter near raft	MODIS
11/08/2019	441.61	20.69	Type-II Plume: next to raft	MODIS
12/08/2019	510.15	87.73	Type-II Plume: near raft	MODIS
13/08/2019	206.13	59.85	Type-II Plume: Surrounding raft	Sentinel-2
14/08/2019	n/a	56.79	None visible – cloudy	MODIS
15/08/2019	n/a	n/a	None visible – cloudy	MODIS
16/08/2019	27.64	108.16	Type-II Plume: around raft	Sentinel-2

4.4.1. Detections at Volcano F

For the 27th September 2001 eruption of Volcano F, we detect the area of the pumice raft to be at least 22 km^2, shown in Fig. 6a, however it is partially covered by cloud, and so is likely an underestimate. There is only one image containing the raft itself — there are cloudy scenes for the next three days and after that the raft is more than 100 km away from Volcano F, and no longer in our study area. There is a blue discoloured seawater area on the 6th of October close to where the raft was travelling but the raft itself is obscured by cloud. From the 5th October onwards there are green plumes above the vent varying between 47 and 472 km^2 until 12th October 2001, shown in Table 5. This eruption was previously detected due to clasts of pumice washing up on beaches and from the detection of eruption-generated T-waves.

For the August 2019 Volcano F eruption, we detect the raft area to be over 185 km^2, shown in Fig. 6c, although there was cloud coverage on the raft on the initial day so the true area is likely to be higher. The raft area decreases with time. The discoloured seawater initial area was around 327 km^2 and increased in the following two days before ceasing to be observable in later dates of satellite imagery, shown in Table 6. The discoloured seawater is mainly to the East of the raft. There was cloud coverage on 13-15/08/2019 so the pumice was not observable between those dates. As shown in Fig. 1, there are further dates in which pumice can be observed from satellite imagery in areas outside of our study region.

Two previously undocumented periods of discoloured seawater were detected at Volcano F between June-August 2020 and in July 2022, detected in the Sentinel-2 imagery due to its higher spatial resolution compared with MODIS. These are shown in Figs. 6e and 7. During the June-August 2020 eruptive period, we observe discoloured seawater on 21/06/2020, 03/07/2020, 31/07/2020 and 15/08/2020, with cloud coverage in between those dates. The maximum area of discoloured seawater detected was 0.38 km^2, significantly less than during the 2001 and 2019 eruptions. For the second newly-detected activity, we observe discoloured seawater on 21/07/2022, of an area of 0.08 km^2 above Volcano F. These results are shown in Table 7, with four Sentinel-2 images, two from directly before and two from directly after to investigate signal duration. There are no signals in the images before or after for the discoloured seawater observed on 21/06/20, 31/07/2020, 15/08/2020 and 21/07/2022. The first images before and after the discoloured seawater observation on 03/07/2020 are cloudy so it is not possible to tell if the signal had a longer duration.

4.4.2. Detections at Home Reef

The 2006 Home Reef eruption released a pumice raft, for which we calculate a maximum area of ~ 370 km^2, shown in Fig. 6b, although we note that this likely underestimates the true total area of the raft due to smaller detached areas of raft misidentified. The images where there are no pumice observations between the 2nd sighting and the final sighting within our study region had extensive cloud coverage over the pumice location, which renders the raft undetectable on those dates. On two of those days, the cloud covered the raft, but did not cover all the discoloured seawater. We detect two separate areas of seawater discolouration – a Type-I Plume directly above the vent and a Type-II plume close to the pumice raft. The total discoloured seawater area

Table 7
Detected areas and descriptions of discoloured seawater and pumice at Volcano F in 2020 and 2022, additionally reporting two Sentinel-2 images pre and post signal.

Date	Discoloured water (km^2)	Pumice (km^2)	Notes	Satellite
16/06/2020	n/a	n/a	None visible – cloudy	Sentinel-2
18/06/2020	0	0	No signal	Sentinel-2
21/06/2020	0.26	0	Point source shaped plume	Sentinel-2
23/06/2020	0	0	No signal	Sentinel-2
26/06/2020	n/a	n/a	None visible – cloudy	Sentinel-2
28/06/2020	n/a	n/a	None visible – cloudy	Sentinel-2
01/07/2020	n/a	n/a	None visible – cloudy	Sentinel-2
03/07/2020	0.38	0	Rounded	Sentinel-2
06/07/2020	n/a	n/a	None visible – cloudy	Sentinel-2
08/07/2020	0	0	No signal	Sentinel-2
26/07/2020	0	0	No signal	Sentinel-2
28/07/2020	n/a	n/a	None visible – cloudy	Sentinel-2
31/07/2020	0.20	0	Elongate swirl	Sentinel-2
02/08/2020	n/a	n/a	None visible – cloudy	Sentinel-2
05/08/2020	n/a	n/a	None visible – cloudy	Sentinel-2
10/08/2020	0	0	No signal	Sentinel-2
12/08/2020	n/a	n/a	None visible – cloudy	Sentinel-2
15/08/2020	0.11	0	Rounded	Sentinel-2
17/08/2020	n/a	n/a	None visible – cloudy	Sentinel-2
20/08/2020	0	0	No signal	Sentinel-2
16/07/2022	0	0	No signal	Sentinel-2
18/07/2022	0	0	No signal	Sentinel-2
21/07/2022	0.084	0	Rounded	Sentinel-2
23/07/2022	0	0	No signal	Sentinel-2
26/07/2022	0	0	No signal	Sentinel-2

increases sharply for the first two days post eruption and then drops again and increases more gradually with time, shown in Table 8. The discoloured seawater (Type-II Plume) on 10/08/2006 is predominantly on the Eastern side of the pumice raft. On 11/08/2006, the discoloured seawater (Type-II Plume) is still mostly to the North-East of the raft but there are additional patches of discoloured seawater to the South of the raft. On 13/08/2006, the raft is mostly covered by cloud but there is some visible discoloured seawater (Type-II Plume) to the east of the raft. The same occurs for 14/08/2006 — the image is mostly covered by cloud but there are smaller patches of discoloured seawater (Type-II Plume) visible, the area likely being an underestimate. The green discoloured seawater (Type-I Plume) area changes shape but remains above the vent of Home Reef. From December 2018 onwards, we observe multiple periods of seawater discolouration above Home Reef volcano. The largest area observed is 22.3 km^2; however, most of the seawater discolouration ranges between 1 and 5 km^2. In October 2022, an island is formed at Home Reef volcano and there is almost continuous seawater discolouration up until the end of 2025.

4.4.3. Spectral properties of discoloured seawater

We show that our detected discoloured seawater patches have spectral signatures that do not align with phytoplankton blooms. In Fig. 8, we show the two previously undetected areas of seawater discolouration above Volcano F, from Sentinel-2 imagery and a MODIS image from the 2001 Volcano F eruption, showing two distinct patches of seawater discolouration. In the Sentinel-2 images, we show higher reflectance in blue, green, red, red edge and NIR, for the plumes compared with background ocean. There is high reflectance in blue and green and there is no significant increase in reflectance between the red and red edge bands. From the 2001 Volcano F eruption, we show the Type-I and Type-II plumes in our MODIS image. Both plumes show increased reflectance in the blue and green bands, compared with background ocean, with the Type-I Plume more reflective in green and the Type-II Plume more reflective in blue. The Type-I Plume shows increased reflectance in red, compared with the Type-II Plume and background ocean. Both plumes and the background ocean exhibit low reflectance in NIR.

5. Discussion

5.1. Spectral pumice sample properties from field spectroscopy

Our pumice hand specimens demonstrate diagnostic dips in IR reflectance when saturated with salt water, shown in Fig. 2. They show a consistent reflectance curve shape, with distinct minima and maxima, in the Volcano F pumice measurements. These distinct maxima and minima are also observed in the other pumice samples, identifying them as characteristic spectral features for pumice. The addition of synthetic saltwater to the samples (dipped and wet conditions) introduces new minima at infrared wavelengths due to water absorption. This is an important insight for remote sensing in marine settings as it demonstrates that it is possible to determine pumice raft saturation in remote sensing data, from satellites with spectral coverage in the range of 1850–2150 nm. The reduced coverage of Sentinel-2 bands for the saltwater-induced minima implies potential limitations in using Sentinel-2 data for detecting pumice saturation. However, data from other satellites, such as Maxar's WorldView-3 (Upchurch and Schott, 2014), could be used for coverage in those parts of the electromagnetic spectrum. The overlap in the B11 and B12 (SWIR) bands in Sentinel-2 provides a window for investigating pumice raft saturation from Sentinel-2 data.

5.1.1. Trends across the Volcano F pumice samples

The reflectance characteristics of the Volcano F pumice samples are consistent across different sample collection locations with differing time at sea, shown in Fig. 2. Their consistency regardless of time spent at sea suggests that exposure to the marine or beach environment over a period of 6 months does not influence their spectral characteristics. The absorption troughs shown at 1400 nm, 1900 nm and the downward trend towards 2500 nm are all indicative of hydration states (Pommerol and Schmitt, 2008; Clark, 1999).

The 1400 nm trough confirms the presence of hydroxyl groups within the mineral structure corresponding to the first overtone of the fundamental O-H stretching vibration. The absorption peak at 1900 nm,

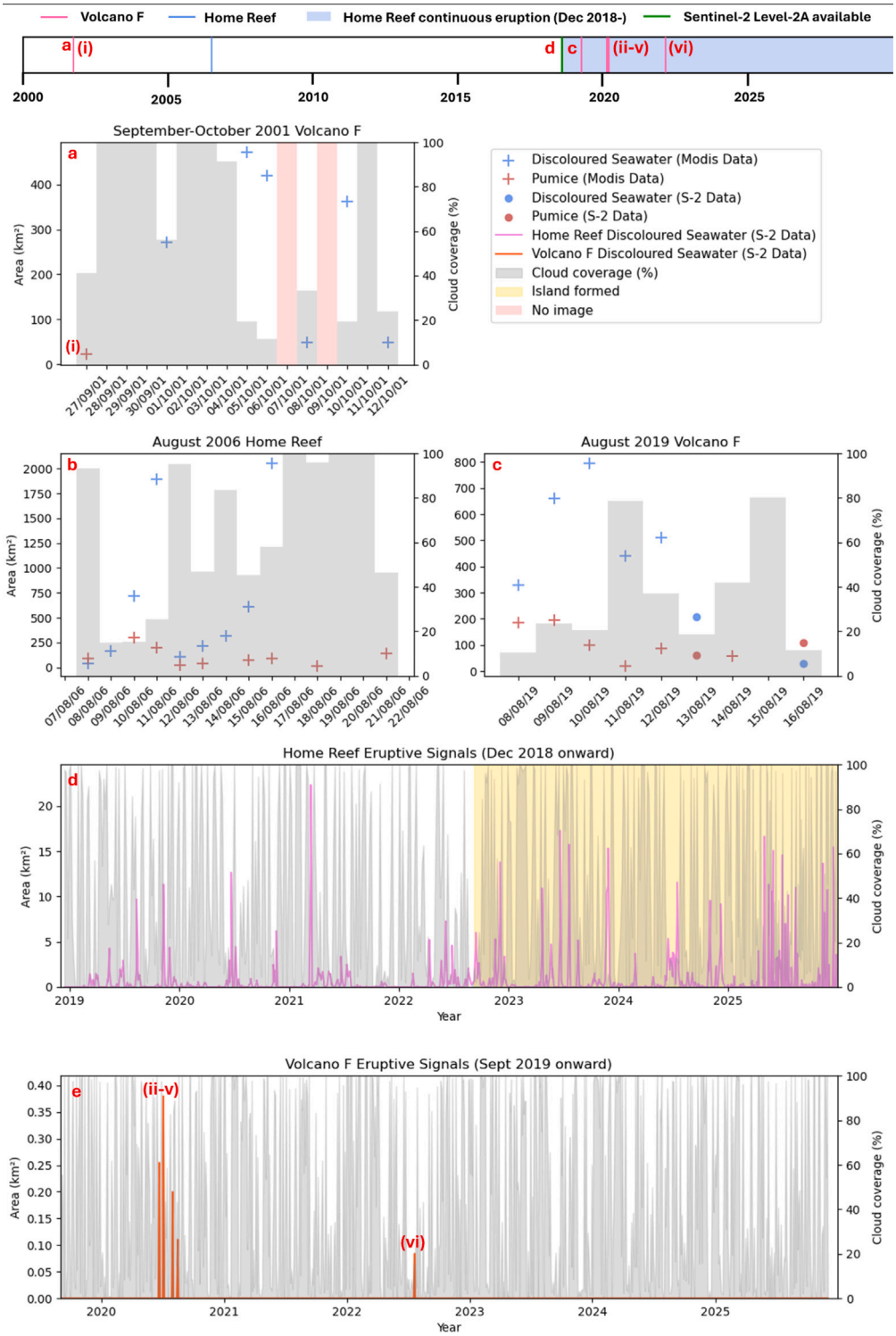


Fig. 6. An eruptive timeline from 2000–2026 of the eruptive events from Volcano F and Home Reef that were flagged in the search area by our random forest algorithm. (a) shows the calculated areas of pumice and discoloured seawater from MODIS imagery during the September-October 2001 eruption of Volcano F, overlayed on cloud coverage percentage of the area 0.3 degrees latitude and longitude surrounding the volcano. (b) and (c) are as in (a) but show data from the 2006 eruption of Home Reef and the 2019 eruption of Volcano F, respectively. (c) contains data points from Sentinel-2 imagery, as well as MODIS imagery. (d) is a time series of the discoloured seawater areas detected at Home Reef Volcano from December 2018 – end of 2025. (e) is a time series of the discoloured seawater areas detected at Volcano F from December 2019 – end of 2025. On the timeline, the roman numerals correspond to satellite images of Volcano F eruptive products shown in Fig. 7: (i) Pumice 27/09/2001, (ii-vi) Discoloured Seawater on 21/06/2020, 03/07/2020, 31/07/2020, 15/08/2020, 21/07/2022.

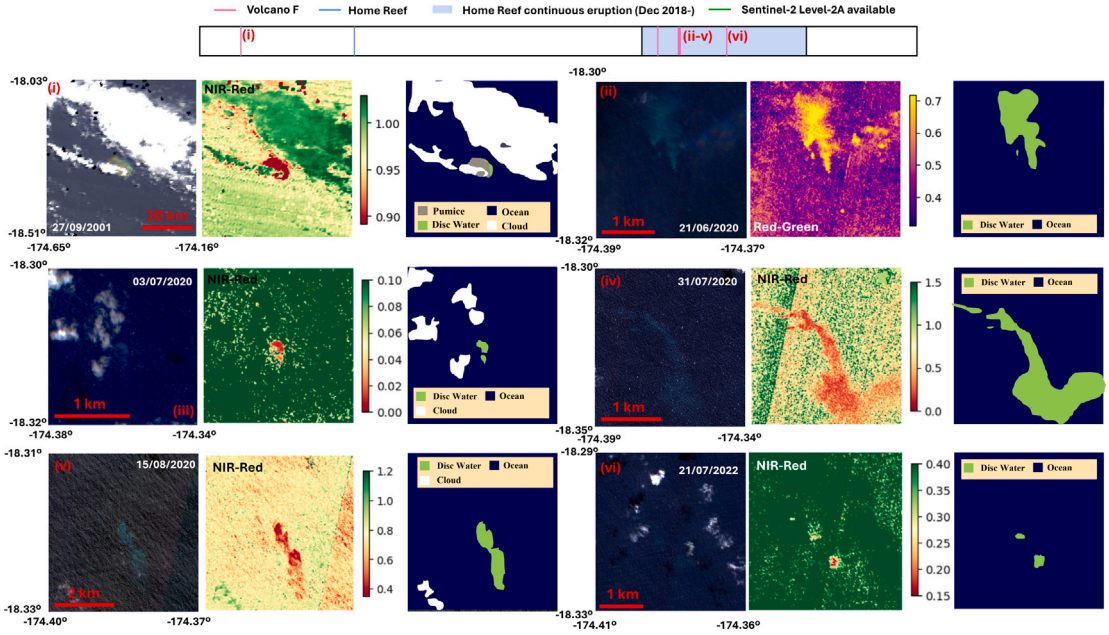


Fig. 7. Shows the same eruptive timeline from 2000–2025 of the eruptive events from Volcano F and Home Reef that were flagged in the search area by our random forest algorithm as in Fig. 6. The timeline contains Roman numerals which correspond to the images on the panels below. (i) shows an RGB MODIS image from 27/09/2001 of the pumice raft and discoloured seawater released in the 2001 eruption of Volcano F. Next to the RGB image is the same image but shown as a false colour ratio of Near Infrared to Red. (ii) shows an RGB Sentinel-2 image of a discoloured seawater plume at Volcano F on 21/06/2020. Next to the RGB image is the same image but shown as a false colour ratio of Red to Green. (iii)-(vi) show RGB Sentinel-2 images of discoloured seawater plumes at Volcano F on 03/07/2020, 31/07/2020, 15/08/2020 and 21/07/2022, respectively. Alongside these images are the same image but shown as a false colour ratio of Near Infrared to Red.

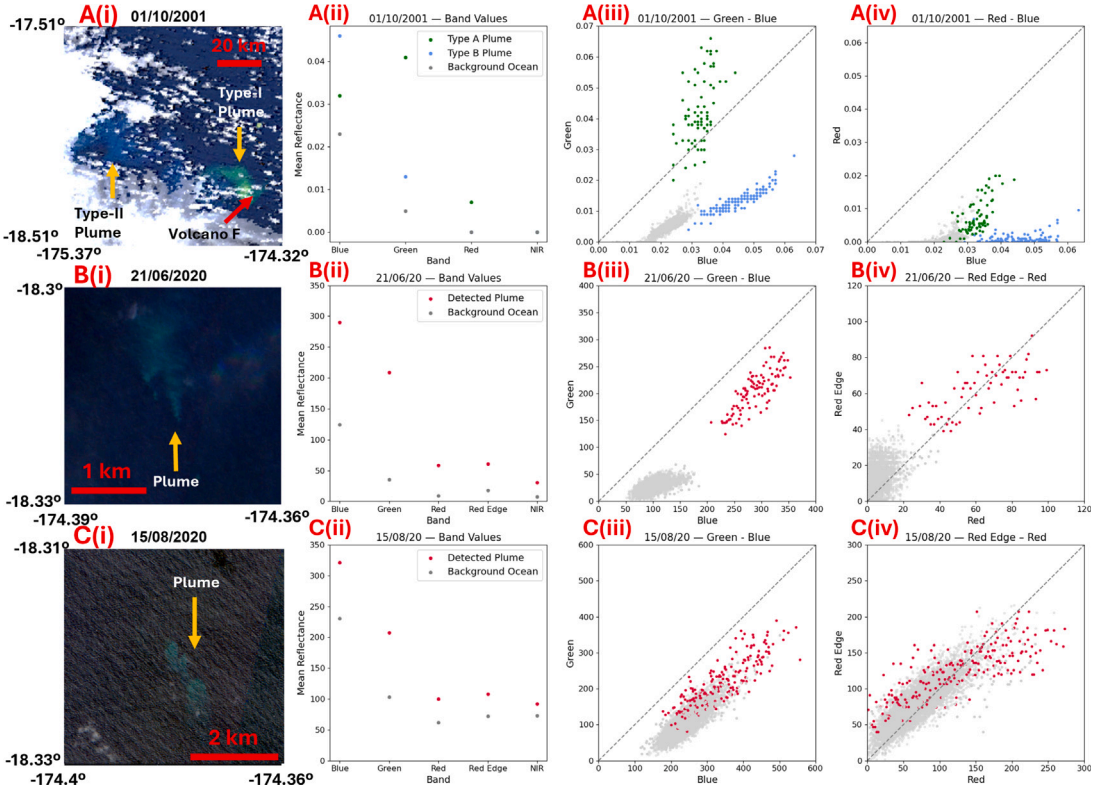


Fig. 8. Average band values across detected areas of seawater discolouration at Volcano F compared with background ocean in a MODIS image (Row A) and two Sentinel-2 images (Rows B and C), displayed in RGB. For the Sentinel-2 images, we plot Green-Blue and Red-Red Edge ratios and for the MODIS image we plot Green-Blue and Red-Blue.

Table 8
Detected areas and descriptions of discoloured seawater and pumice during the 2006 Home Reef eruption.

Date	Discoloured water (km^2)	Pumice (km^2)	Notes	Satellite
08/08/2006	37.63	90.22	Partially obscured by cloud	MODIS
09/08/2006	163.74	n/a	Type-II Plume, raft obscured by cloud	MODIS
10/08/2006	716.03	296.08	Type-I Plume close to vent, Type-II Plume: surrounding raft	MODIS
11/08/2006	1890.11	195.63	Type-II Plume: surrounding raft, vent is not in image	MODIS
12/08/2006	102.68	23.92	Type-II Plume: surrounding raft, vent is covered by cloud	MODIS
13/08/2006	217.81	40.62	Cloudy image	MODIS
14/08/2006	319.73	123.90	Type-I plume: at vent - yellow-green colour, Type-II Plume: around raft	MODIS
15/08/2006	611.54	71.03	Type-I Plume: above vent, Type-II Plume: surrounding raft	MODIS
16/08/2006	2050.17	91.46	Type-I plume: above vent, Type-II Plume: surrounding raft	MODIS
17/08/2006	n/a	n/a	Cloudy image	MODIS
18/08/2006	n/a	17.69	Cloudy image	MODIS
19/08/2006	n/a	n/a	No image	MODIS
20/08/2006	n/a	n/a	Cloudy image	MODIS
21/08/2006	n/a	137.45	Cloudy image	MODIS

indicative of intact molecular H_2O within the crystal structures (Pommerol and Schmitt, 2008; Clark, 1999). This occurs due to a quantum mechanical combination band coupling two mid-infrared vibrational modes within the water molecule: the O-H stretching vibration (ν_1 or ν_3 occurring around 2700–2800 nm and the H-O-H bending vibration (ν_2, occurring near 6100 nm) (Clark, 1999). The downward trend towards 2500 nm is the 'shoulder' of the large absorption peak caused by the asymmetric and symmetric stretching bands of O-H centred around 3000 nm, which suppresses the overall continuum reflectance spectrum (Craig et al., 2006). These distinct absorption troughs shown are important as they can be used to remotely measure raft saturation, helping to determine the remaining time before the raft becomes submerged.

5.1.2. Trends in pumice samples from other settings

Across our samples, we demonstrate that pumice has a consistent and identifiable spectral signature, despite differences in composition and weathering state. Though these differences are observed in the spectra, the overall spectral form is consistent across all forms of pumice, shown in Fig. 2. Darker, iron-rich pumices show lower reflectance (Holuhraun sample), whereas high silica, low iron pumices (Mt Hekla, Havre, Kolumbo) show a higher reflectance. Some of the samples (Melimoyu, Mt Hekla) display reflectance troughs due to secondary alteration processes like hydration. These observations suggest that, while spectral details vary with composition and alteration, the general spectral signature of pumice is sufficiently consistent to suggest generalisation across different eruptions and settings.

The unique spectral shape and high reflectance of the Kolumbo pumice, a rhyolitic pumice, is due to its high-silica and low-iron content. These features all increase light scattering and suppress darker absorption features shown in less glassy or more iron-rich pumices. Havre's high surface roughness and low iron content both increase reflectivity. The clast itself is white, showing a high reflectance in the visible bands. Mt Hekla pumice is silicic leading to high reflectance. The similar absorption peak observed in the wet Volcano F samples and the Melimoyu and Mount Hekla samples suggest that long-term hydration has taken place in the history of these samples. This is shown in absorption peaks at 1.9 μm, indicative of intact molecular H_2O within the crystal structures (Pommerol and Schmitt, 2008; Clark, 1999).

The spectra capture a diverse range of contributing factors, reflecting variations in surface roughness and composition. This leads to opportunities for more comprehensive studies. For example, including more pumice samples from different settings and multiple pumices from the same settings would improve our understanding of the spectral signature changes across pumices. Previous work has shown that pumice properties evolve during transport (Jutzeler et al., 2014; Manga et al., 2018), and can depend on grain size and surface condition (Ishimura and Hiramine, 2025). This would ideally be done with samples taken directly from a pumice raft, reducing external environmental impacts. Rapid-response sampling campaigns have proven effective in past raft events and would allow acquisition of minimally altered clasts (Jutzeler et al., 2020). Further, linking spectral measurements to specific surface textures would provide a more mechanistic understanding of spectral variability. High-resolution imaging techniques such as Scanning Electron Microscope (SEM) have been used to quantify pumice microtextures, vesicle morphologies, and abrasion features (Pistolesi et al., 2021). Combining SEM-derived textural metrics with field spectroscopy would enable direct assessment of how micro-scale roughness, vesicle exposure, and fine-material coatings influence reflectance behaviour.

5.2. Field spectroscopy comparison of Volcano F pumice with other types of floating debris

The comparison of field spectroscopy measurements shows that Volcano F pumice exhibits a spectral reflectance curve that is clearly distinct from other floating debris types, shown in Fig. 3. Despite oil, plastics, and driftwood displaying strong absorption features corresponding to water presence (at 1400 nm, 1900 nm, and 2500 nm) like the wet and dipped pumice, the curves show a diverse range of features that provide differentiation. These pronounced differences in reflectance are also evident viewing the data as Sentinel-2 would and pumice retains a characteristic multispectral shape that is not replicated by oil, plastics, or driftwood. This suggests that pumice rafts should remain spectrally identifiable in Sentinel-2 imagery despite moisture variation, surface wetting, or the coarse spectral resolution of MSI. The persistence of pumice's diagnostic curve across measurement spaces provides strong evidence that pumice can be reliably separated from other floating debris using multispectral satellite data.

5.3. Physical pumice clast properties

The Lakeba samples (465 km from the vent) show systematically larger clast areas and lower circularity than those collected at Yasawa (850 km), shown in Fig. 4. This spatial trend suggests that pumice clasts undergo measurable physical modification during transport (Jutzeler et al., 2020; Redick, 2023). Larger, more angular clasts near the vent likely reflect the initial fragmentation state of the raft, where pumice pieces have experienced limited abrasion and retain irregular outlines

from eruptive processes. As the raft drifts, clasts repeatedly collide, abrade, and fracture, producing smaller and more rounded fragments. The higher mean circularity at Yasawa (0.706 vs. 0.654 at Lakeba) is consistent with this interpretation, as rounding is a well-documented outcome of sustained inter-clast interaction in floating pumice rafts. We note that Ishimura and Hiramine (2025) document how grain size affects changes in shape of pumice clasts. We did not incorporate grain-size standardisation in our analysis and instead report the shape metrics directly from the measured clasts. We depict these results in Panels B and C of Fig. 9.

5.4. Spectral raft properties from satellite imagery

We interpret the increased visible-band reflectance and decreased SWIR-derived temperature towards the raft margins, shown in Fig. 5, as evidence of thinner raft margins and pumice accumulation towards the centre of the raft leading to raised topography. Thinner raft margins, where pumice clasts break off from, sit lower in and partially within the water column, leading to increased scattering in RGB by the water column and decreased SWIR reflectance. Our field spectroscopy data from Fig. 2 demonstrates the decrease in SWIR reflectance with increased pumice saturation, however RGB scattering reflectance also decreases with saturation. For our wet field spectroscopy data, the pumice samples were measured as isolated solid wet surfaces, with no potential for water column scattering hence leading to lower RGB reflectance. It follows that a thicker pumice centre likely forms slightly raised, drier surfaces, leading to observations of both lower reflectance in the visible bands, with no water column scattering, and higher SWIR reflectance relative to the raft margins.

Another possible explanation that increases the reflectance in the visible bands is that the raft surface roughness increases towards the edge of the raft leading to increased scattering in the visible bands. At 10 m spatial resolution, we cannot resolve individual clast roughness but larger-scale changes in surface roughness likely affect the overall reflectance. The edge effect becomes less pronounced over time suggesting an increased uniformity of the raft either in terms of topography or in surface roughness. The general decrease in all spectral values over time indicates an increase in raft saturation. However, despite the edge effects and general decrease in reflectance, the spectral properties of the raft remain stable enough over time to be characteristically identified as pumice. We depict these results in Panel A of Fig. 9.

5.5. Automated eruption detection

We demonstrate the successful use of machine learning to provide systematic satellite-based eruptive histories of activity at Volcano F and Home Reef over a 25-year period. The eruptive activity detected by our random forest algorithm include large area pumice raft forming events and smaller areas of seawater discolouration, shown in Figs. 6 and 7.

Here we discuss the possible sources of the seawater discolouration and whether it is viable to interpret them as having a volcanic origin. The most likely sources for seawater discolouration unrelated to volcanic activity are naturally occurring phytoplankton blooms, river discharge into oceans and shallow water surrounding island formations. We can rule out discolouration due to river discharge and shallow water due to those not being present in our study region. The discoloured seawater above and surrounding Home Reef volcano frequently coincides with other volcanic sequences — subaerial plumes and the formation of a volcanic island. Local reports from the Tonga Geological Services coincide with eruptive events detected in our study (Global Volcanism Program, 2024).

At Volcano F, for the 2001 and 2019 eruptive events, the presence of a pumice raft confirms eruptive activity. For our seawater discolouration detections in 2020 and 2021, there are no other co-inciding volcanic signals to help evidence an eruptive sequence. Our spectral analysis of the discoloured seawater patches above the Volcano F vent shows a different spectral signature to the distinctive spectral signature of phytoplankton, shown in Fig. 8. Specifically, the lack of a significant increase in red edge reflectance from red reflectance in both the 2020 plumes compared with background ocean shows this. There is no chlorophyll-a data from the 2001 Volcano F eruption as MODIS Aqua satellite launched in 2002, however during the 2006 Home Reef eruption, there are no significant ocean colour anomalies attributed to higher chlorophyll concentrations (Mantas et al., 2011). Further, naturally occurring phytoplankton blooms occur during the summer months – December, January, February – whereas our detections are all during June – August, (Hermilly et al., 2025). The detected shapes of our seawater discolouration are suggestive of a plume-like geometry from a point source, especially on 21/06/2020. Phytoplankton blooms formed naturally by non-volcanic sequences display more spatially diffuse structures (IOCCG, 2014). Hence, we demonstrate the plumes are unlikely of naturally occurring phytoplankton and therefore likely to be of volcanic origin.

The observation of two distinct discoloured seawater plumes during the 2006 Home Reef and Volcano F 2001 eruptions and their associated locations suggest different processes are occurring affecting seawater colour. Above the vent, we attribute Type-I Plumes as consisting of SiO_2, Al_2O_3 and Fe_2O_3, with the greenish colour corresponding to higher Fe and Al contributions (Urai and Machida, 2005). The Type-II Plumes we observe around the pumice raft are thought to be caused by fine size pumice particles suspended in the water column (Mantas et al., 2011). This two plume type pattern was previously reported at Home Reef in 2006 (Mantas et al., 2011), our observations of this pattern at Volcano F too indicate that the process may be more widespread. We describe the two plume types in Panels D and E of Fig. 9.

Our maximum area estimate of the 2006 Home Reef pumice raft ($\sim$ 370 km^2) on 10/08/2006 is less than the 440 km^2 reported by Global Volcanism Program (2024) from the same satellite image. The SGVP area report was based on a manually drawn MODIS mask (BGVN 31:10). Differences between these values reflect methodological choices, manual masks tend to include ambiguous or mixed pixels, whereas automated classifiers apply stricter spectral thresholds and therefore produce more conservative area estimates (excluding, for example, pumice obscured by patchy cloud). The evolution over time of the discoloured seawater patches, a rapid increase followed by fluctuating activity suggests that this event may have had multiple eruptive periods, not just the event that produced the raft. We encounter difficulties with cloud coverage of the eruptive signals on specific days. The formation of a new island and sustained discoloured seawater patches surrounding Home Reef indicate continuous eruptive activity, however the areas are smaller than that of the major 2006 eruption suggesting they are more minor background activity rather than a large eruptive event.

The 2001 raft satellite coverage is limited by cloud coverage, suggesting the true size of the raft may be larger. The detection of the 2019 eruption of Volcano F demonstrates the robustness of our algorithm for the tracking pumice raft events, even when the raft is fragmented or partially covered by cloud. We measure the raft to be 185 km squared, which aligns with measurements of 195 km^2 from Brandl et al. (2020), Jutzeler et al. (2020). The detection of two previously undocumented periods of discoloured seawater (June-August 2020 and July 2022) at Volcano F in Sentinel-2 imagery indicates that Volcano F is more active than previously thought and may have erupted more during the 25-year period. Access to high spatial resolution satellite imagery, on the scale of Sentinel-2, would answer questions about the frequency of eruptive signals pre-2018, however there is no Sentinel-2 Level 2A data pre-2018. This shows the importance of use and access to high spatial resolution imagery for the detection of smaller scale eruptions. Further, it raises the question of how many submarine volcanic events are occurring undetected at submarine volcanoes.

Eruptions were unable to be detected fairly frequently due to high cloud coverage in the Sentinel-2 and MODIS images. Using this data

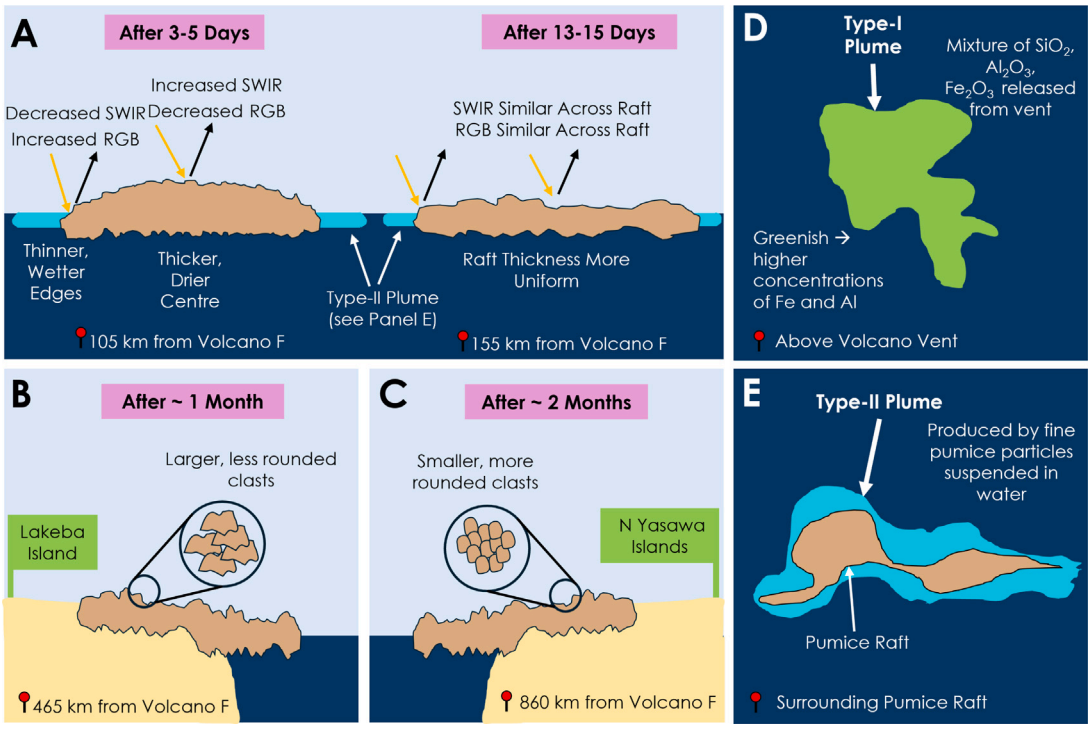


Fig. 9. Schematic figure describing some key results from this study. Panel A shows the raft becoming more uniform over time. Panels B and C show the decrease in clast size and increase in clast roundness over time. Panels D and E describe Types-I and II Plumes.

combined with training an automated algorithm on radar imagery may help to avoid this problem, however the Sentinel-1 coverage is sparse in this region. Sentinel-1 has better coverage in coastal regions so it may work better for coastal submarine eruptions. The incorporation of additional datasets such as surface windspeed and image texture would improve our detection algorithm, alongside increasing the size of our training dataset. Here we have demonstrated the potential for automated detection and tracking of submarine eruptions. Submarine eruptions occur in remote regions, with little-to-no in-situ monitoring, therefore applying our methods in wider geographical regions could reveal significant undocumented submarine activity.

5.6. Comparison with previous work

Satellite-based analyses of pumice rafts have expanded rapidly in recent years. Studies such as (He et al., 2025) have demonstrated the value of Sentinel-2 and machine-learning approaches for quantifying raft behaviour, including daily changes in areal extent across multiple events. Similarly, Zheng et al. (2022) applied supervised classification methods to identify previously undocumented rafts in the Rabaul region. Other major contributions have focused on raft morphology, dispersal pathways, and clast transport using MODIS and other sensors (e.g. Jutzeler et al. (2014, 2020), Yeo et al. (2024), Carey et al. (2014), Manga et al. (2018)). At the clast scale, SEM-based studies have characterised pumice microtextures, abrasion features, and vesicle exposure (Pistolesi et al., 2021), while recent work has investigated grain size, shape and petrological characteristics of clasts (Ishimura and Hiramine, 2025; Yoshida et al., 2022).

Although these studies have substantially advanced our understanding of pumice-raft behaviour, they generally treat raft-scale satellite observations and clast-scale physical properties separately. Our work builds on this by examining the 2019 Volcano F eruption through a combined remote-sensing and sample-based approach. We relate satellite-derived spectral changes to laboratory measurements of pumice reflectance demonstrating that raft-scale spectral variations can be used to infer broad physical changes in raft characteristics. In addition, applying long-term random forest classifiers to 25 years of MODIS and 7 years of Sentinel-2 imagery provides a more complete eruptive record for Volcano F and Home Reef, including several events previously undocumented. This integrated perspective complements earlier studies and offers a framework for linking raft evolution with the physical characteristics of the pumice involved.

6. Conclusion

Our study shows that through the integration of remote sensing, field measurements and machine-learning approaches, we can significantly increase our understanding of submarine volcanic processes and their eruptive products. We show that pumice samples have a spectral reflectance signature distinctive to pumice and identify that silica content, surface roughness and iron content are key factors affecting variation across samples from different volcanoes. We also compare our pumice spectra to spectra of other floating debris to demonstrate spectral differences. Our transect analyses demonstrate that it is possible to remotely observe an increase in raft saturation with time spent in the sea. As summarised in Fig. 9, the raft appears to become more uniform the longer it floats for, initially it has a thicker centre but this soon decreases. The raft also changes shape and travels rapidly post eruption. Our data suggests that pumice samples collected further away from the eruptive vent, with longer time spent at sea, are more eroded although their circularity remains similar regardless of collection location.

We successfully use supervised machine learning to identify both major and minor, documented and undocumented eruptions over a 25-year time span at Volcano F and Home Reef. We identify two periods

of previously undetected submarine activity at Volcano F, and satellite evidence of a documented eruption previously thought to have no coverage. We detect the major 2006 eruption and continuous fluctuations in minor eruptive events at Home Reef, and show that these areas of seawater discolouration are likely due to volcanic sources.

CRediT authorship contribution statement

Alice M. Hopkins: Writing – original draft, Visualization, Software, Methodology, Investigation, Formal analysis, Data curation. **Susanna K. Ebmeier:** Writing – review & editing, Supervision, Methodology, Conceptualization. **Timothy J. Craig:** Writing – review & editing, Supervision. **Isobel A. Yeo:** Writing – review & editing, Supervision.

Open research

The satellite imagery used in this study is all freely available through Google Earth Engine. The pumice hyperspectral data measured in our study is available on request.

Declaration of competing interest

The authors declare that they have no known competing financial interests or personal relationships that could have appeared to influence the work reported in this paper.

Acknowledgements

We thank the Natural Environmental Research Council (NERC) Field Spectroscopy Facility for the loan of the SVC HR-1024i Field Spectrometer and for providing assistance in the field spectrometry analysis. We thank Dr Iona M. McIntosh for the loan of the Volcano F pumice samples. We thank members of the Institute of Geophysics and Tectonics at University of Leeds for excitedly contributing their pumice samples for analysis. We use Generic Mapping Tools (GMT) 6.0 (Wessel et al., 2019) and Matplotlib (Hunter, 2007) for data visualisation. We use QGIS (Rosas-Chavoya et al., 2022) for the creation of our training dataset and use Google Earth Engine (Gorelick et al., 2017) for the Machine Learning analysis and all the satellite imagery used. We use ImageJ (Schneider et al., 2012) for analysis of our pumice samples. AMH is funded by NERC through a SENSE 1024 CDT studentship (NE/T00939X/1). SKE is funded by a NERC Independent Research 1026 Fellowship (NE/R015546/1). TJC is funded by the Royal Society under URF\R1\180088, URF\R\231019. IAY acknowledges NERC funding from NE/T010916/1 (for the pumice collection), NE/X00239X/1 and NE/X003272/1. AMH, SKE, and TJC are members of COMET, which is the NERC Centre for the Observation and Modelling of Earthquakes, Volcanoes and Tectonics, a partnership between UK Universities and the British Geological Survey.

Appendix A. Supplementary data

Supplementary material related to this article can be found online at https://doi.org/10.1016/j.jvolgeores.2026.108751.

Data availability

The satellite imagery used in this study is all freely available through Google Earth Engine. The pumice hyperspectral data measured in our study is available on request.

References

Akiyama, Y., Okada, T., Yuhara, T., 2022. Observations of mobile macro-epifauna on pumice rafts generated by Fukutoku-Oka-no-Ba volcano in Oku Port, Okinawa Prefecture. Aquat. Anim. 2022, AA2022–13.

Borrero, J.C., Cronin, S.J., Latu'ila, F.H., Tukuafu, P., Heni, N., Tupou, A.M., Kula, T., Fa'anunu, O., Bosserelle, C., Lane, E., Lynett, P., Kong, L., 2023. Tsunami runup and inundation in Tonga from the January 2022 eruption of Hunga volcano. Pure Appl. Geophys. 180 (1), 1–22. http://dx.doi.org/10.1007/s00024-022-03215-5.

Boyd, P.W., Jickells, T., Law, C.S., Blain, S., Boyle, E.A., Buesseler, K.O., Coale, K.H., Cullen, J.J., de Baar, H.J.W., Follows, M., Harvey, M., Lancelot, C., Levasseur, M., Owens, N.P.J., Pollard, R., Rivkin, R.B., Sarmiento, J., Schoemann, V., Smetacek, V., Takeda, S., Tsuda, A., Turner, S., Watson, A.J., 2007. Mesoscale iron enrichment experiments 1993–2005: Synthesis and future directions. Science 315 (5812), 612–617. http://dx.doi.org/10.1126/science.1131669, American Association for the Advancement of Science, URL https://www.science.org/doi/10.1126/science.1131669.

Brandl, P.A., Schmid, F., Augustin, N., Grevemeyer, I., Arculus, R.J., Devey, C.W., Petersen, S., Stewart, M., Kopp, H., Hannington, M.D., 2020. The 6–8 Aug 2019 eruption of 'volcano F' in the Tofua Arc, Tonga. J. Volcanol. Geotherm. Res. 390, 106695. http://dx.doi.org/10.1016/j.jvolgeores.2019.106695, URL https://www.sciencedirect.com/science/article/pii/S0377027319305098.

Brewin, R.J.W., Ciavatta, S., Sathyendranath, S., Skákala, J., Bruggeman, J., Ford, D., Platt, T., 2019. The influence of temperature and community structure on light absorption by phytoplankton in the North Atlantic. Remote Sens. Environ. 228, 1–13. http://dx.doi.org/10.1016/j.rse.2019.04.019.

Browning, T.J., Bouman, H.A., Henderson, G.M., Mather, T.A., Pyle, D.M., Schlosser, C., Woodward, E.M.S., Moore, C.M., 2014. Strong responses of Southern Ocean phytoplankton communities to volcanic ash. Geophys. Res. Lett. 41 (8), 2851–2857. http://dx.doi.org/10.1002/2014GL059364, URL https://agupubs.onlinelibrary.wiley.com/doi/full/10.1002/2014GL059364.

Bryan, S.E., Cook, A., Evans, J.P., Colls, P.W., Wells, M.G., Lawrence, M.G., Jell, J.S., Greig, A., Leslie, R., 2004. Pumice rafting and faunal dispersion during 2001–2002 in the Southwest Pacific: Record of a dacitic submarine explosive eruption from Tonga. Earth Planet. Sci. Lett. 227 (1), 135–154. http://dx.doi.org/10.1016/j.epsl.2004.08.009, URL https://www.sciencedirect.com/science/article/pii/S0012821X0400500X.

Bryan, S.E., Cook, A.G., Evans, J.P., Hebden, K., Hurrey, L., Colls, P., Jell, J.S., Weatherley, D., Firn, J., 2012. Rapid, long-distance dispersal by Pumice rafting. PLOS ONE 7 (7), e40583. http://dx.doi.org/10.1371/journal.pone.0040583, Publisher: Public Library of Science, URL https://journals.plos.org/plosone/article?id=10.1371/journal.pone.0040583.

Cahalan, R., Dufek, J., 2021. Explosive submarine eruptions: The role of condensable gas jets inunderwater eruptions. J. Geophys. Res.: Solid Earth http://dx.doi.org/10.1029/2020JB020969.

Carey, R.J., Wysoczanski, R., Wunderman, R., Jutzeler, M., 2014. Discovery of the largest historic silicic submarine eruption. Eos, Trans. Am. Geophys. Union 95 (19), 157–159. http://dx.doi.org/10.1002/2014EO190001, _eprint: https://onlinelibrary.wiley.com/doi/pdf/10.1002/2014EO190001, URL https://onlinelibrary.wiley.com/doi/abs/10.1002/2014EO190001.

Chen, X., Sun, S., Zhao, J., Ai, B., 2022. Spectral discrimination of pumice rafts in optical MSI imagery. Remote. Sens. 14 (22), 5854. http://dx.doi.org/10.3390/rs14225854, Number: 22 Publisher: Multidisciplinary Digital Publishing Institute, URL https://www.mdpi.com/2072-4292/14/22/5854.

Ciancia, E., Marchese, F., Mazzeo, G., Plank, S., Pergola, N., 2026. A spectrally-derived method for detecting sea-water discoloration around submarine volcanoes in oligotrophic oceans by integrating Sentinel-2A/B-MSI and Landsat 8/9-OLI data. Marine Poll. Bull. 225, 119266. http://dx.doi.org/10.1016/j.marpolbul.2026.119266, URL https://www.sciencedirect.com/science/article/pii/S0025326X26000536.

Clark, R.N., 1999. Spectroscopy of rocks and minerals, and principles of spectroscopy. In: Rencz, A.N. (Ed.), Manual of Remote Sensing: Remote Sensing for the Earth Sciences, third ed. vol. 3, John Wiley & Sons, New York, pp. 3–58.

Colombier, M., Bonifacie, M., Brenna, M., et al., 2025. The role of submarine volcanism in atmospheric chemistry. Earth Planet. Sci. Lett. http://dx.doi.org/10.1016/j.epsl.2025.119690.

Cox, E., 1927. A method of assigning numerical and percentage values to the degree of roundness of sand grains. J. Paleontol. 179–183.

Craig, M., Cloutis, E., Kaletzke, L., McCormack, K., Stewart, L., 2006. Alteration of hydration absorption features in reflectance spectra of selected sulfates in a low pressure environment: 0.45–4.3μm. In: 37th Annual Lunar and Planetary Science Conference. p. 2112.

Cronin, J.F., 1971. Recent volcanism and the stratosphere. Science 172, http://dx.doi.org/10.1126/science.172.3985.847.

de Maisonneuve, C., Forni, F., Bachmann, O., 2021. Magma reservoir evolution during the build up to and recovery from caldera-forming eruptions–a generalizable model? Earth-Sci. Rev. 218, 103684. http://dx.doi.org/10.1016/j.earscirev.2021.103684, _eprint: https://www.sciencedirect.com/science/article/pii/S0012825220304640/pdfft, URL https://www.sciencedirect.com/science/article/pii/S0012825220304640.

Drusch, M., Del Bello, U., Carlier, S., Colin, O., Fernandez, V., Gascon, F., Hoersch, B., Isola, C., Laberinti, P., Martimort, P., Meygret, A., Spoto, F., Sy, O., Marchese, F., Bargellini, P., 2012. Sentinel-2: ESA's optical high-resolution mission for GMES operational services. Remote Sens. Environ. 120, 25–36. http://dx.doi.org/10.1016/j.rse.2011.11.026, URL https://www.sciencedirect.com/science/article/pii/S0034425712000636.

Elser, J., Bastidas Navarro, M., Corman, J., Emick, H., Kellom, M., Laspoumaderes, C., Lee, Z., Poret-Peterson, A., Balseiro, E., Modenutti, B., 2015. Community structure and biogeochemical impacts of microbial life on floating pumice. Appl. Environ. Microbiol. http://dx.doi.org/10.1128/AEM.03160-14.

Eugenio, F., Martin, J., Marcello, J., Fraile-Nuez, E., 2014. Environmental monitoring of El Hierro Island submarine volcano, by combining low and high resolution satellite imagery. Int. J. Appl. Earth Obs. Geoinf. 29, 53–66. http://dx.doi.org/10.1016/j.jag.2013.12.009.

European Union/ESA/Copernicus, 2025. Copernicus S2 SR harmonized — Harmonized sentinel-2 MSI level-2A surface reflectance (Version X). Copernicus/ESA, Accessed 19 August 2025.

Fingas, M., 2021. Visual appearance of oil on the sea. J. Mar. Sci. Eng. 9 (1), http://dx.doi.org/10.3390/jmse9010097, URL https://www.mdpi.com/2077-1312/9/1/97.

Fingas, M., Fieldhouse, B., 2004. Formation of water-in-oil emulsions and application to oil spill modelling. J. Hazard. Mater. 107 (1), 37–50. http://dx.doi.org/10.1016/j.jhazmat.2003.11.008, URL https://www.sciencedirect.com/science/article/pii/S0304389403004114.

Geist, D., 2021. Hekla revisited: Fractionation of a magma body at historical timescales. J. Petrol. 62 (8), egab001. http://dx.doi.org/10.1093/petrology/egab001.

Geoffroy, C.A., 2018. A widespread compositionally bimodal tephra sourced from Volcán Melimoyu (44°S, Northern Patagonian Andes): Insights into magmatic reservoir processes and opportunities for regional correlation. Quat. Sci. Rev. 200, 141–159. http://dx.doi.org/10.1016/j.quascirev.2018.09.034, URL https://www.sciencedirect.com/science/article/pii/S0277379118305511.

Global Volcanism Program, 2024. Volcanoes of the world (v. 5.2.5; 23 Dec 2024). http://dx.doi.org/10.5479/si.GVP.VOTW5-2024.5.2, Distributed by Smithsonian Institution, compiled by Venzke, E..

Gorelick, N., Hancher, M., Dixon, M., Ilyushchenko, S., Thau, D., Moore, R., 2017. Google earth engine: Planetary-scale geospatial analysis for everyone. Remote Sens. Environ. 202, 18–27. http://dx.doi.org/10.1016/j.rse.2017.06.031, URL https://www.sciencedirect.com/science/article/pii/S0034425717302900.

Halldórsson, S.A., 2018. Petrology and geochemistry of the 2014–2015 Holuhraun eruption, central Iceland: Compositional and mineralogical characteristics, temporal variability and magma storage. Contrib. Miner. Pet. 173, 64. http://dx.doi.org/10.1007/s00410-018-1487-9.

He, S., Qi, L., Wang, M., Le, C., Hu, C., 2025. Pumice rafts in the global ocean: A remote sensing assessment. GIScience & Remote. Sens. 62 (1), 2555093. http://dx.doi.org/10.1080/15481603.2025.2555093.

Helo, C., Longpré, M., Shimizu, N., et al., 2011. Explosive eruptions at mid-ocean ridges driven by CO2-rich magmas. Nat. Geosci 4, 260–263. http://dx.doi.org/10.1038/ngeo1104, URL https://www.nature.com/articles/ngeo1104#citeas.

Hermilly, T., Martinez, E., Uitz, J., Cornec, M., Kolodziejczyk, N., Schmechtig, C., 2025. Seasonal variability of phytoplankton vertical distribution in a contrasted South Pacific Ocean from BioGeoChemical-argo profiling floats. Geophys. Res. Lett. 52, http://dx.doi.org/10.1029/2024GL114262, e2024GL114262.

Hersbach, H., Bell, B., Berrisford, P., Hirahara, S., Horányi, A., Muñoz-Sabater, J., Nicolas, J., Peubey, C., Radu, R., Schepers, D., Simmons, A., Soci, C., Abdalla, S., Abellan, X., Balsamo, G., Bechtold, P., Biavati, G., Bidlot, J., Bonavita, M., De Chiara, G., Dahlgren, P., Dee, D., Diamantakis, M., Dragani, R., Flemming, J., Forbes, R., Fuentes, M., Geer, A., Haimberger, L., Healy, S., Hogan, R., Hólm, E., Janisková, M., Keeley, S., Laloyaux, P., Lopez, P., Lupu, C., Radnoti, G., de Rosnay, P., Rozum, I., Vamborg, F., Villaume, S., Thépaut, J.-N., 2020. ERA5 hourly data on single levels from 1979 to present. http://dx.doi.org/10.24381/cds.adbb2d47, Copernicus Climate Change Service (C3S).

Houghton, B.F., Wilson, C.J.N., 1989. A vesicularity index for pyroclastic deposits. Bull. Volcanol. 51 (6), 451–462. http://dx.doi.org/10.1007/BF01078811.

Hunter, J.D., 2007. Matplotlib: A 2D graphics environment. Comput. Sci. Eng. 9 (03), 90–95. http://dx.doi.org/10.1109/MCSE.2007.55, Publisher: IEEE Computer Society, URL https://www.computer.org/csdl/magazine/cs/2007/03/c3090/13rRUwbJD0A.

IOCCG, 2014. Phytoplankton Functional Types from Space. Technical Report IOCCG Report 15, International Ocean Colour Coordinating Group, URL https://ioccg.org/wp-content/uploads/2018/09/ioccg_report_15_2014.pdf.

Ishimura, D., Hiramine, R., 2025. Dispersion, fragmentation, abrasion, and organism attachment of drift pumice from the 2021 Fukutoku-Oka-no-Ba eruption in Japan. Prog. Earth Planet. Sci. 12 (1), 5.

Justice, C.O., Townshend, J.R.G., Vermote, E.F., Masuoka, E., Wolfe, R.E., Saleous, N., Roy, D.P., Morisette, J.T., 2002. An overview of MODIS land data processing and product status. Remote Sens. Environ. 83 (1), 3–15. http://dx.doi.org/10.1016/S0034-4257(02)00084-6, URL https://www.sciencedirect.com/science/article/pii/S0034425702000846.

Jutzeler, M., Marsh, R., Carey, R.J., White, J.D.L., Talling, P.J., Karlstrom, L., 2014. On the fate of pumice rafts formed during the 2012 Havre submarine eruption. Nat. Commun. 5 (1), 3660. http://dx.doi.org/10.1038/ncomms4660, Number: 1 Publisher: Nature Publishing Group, URL https://www.nature.com/articles/ncomms4660.

Jutzeler, M., Marsh, R., van Sebille, E., Mittal, T., Carey, R.J., Fauria, K.E., Manga, M., McPhie, J., 2020. Ongoing dispersal of the 7 August 2019 pumice raft from the Tonga Arc in the Southwestern Pacific Ocean. Geophys. Res. Lett. 47 (5), e1701121. http://dx.doi.org/10.1029/2019GL086768, _eprint: https://onlinelibrary.wiley.com/doi/pdf/10.1029/2019GL086768, URL https://onlinelibrary.wiley.com/doi/abs/10.1029/2019GL086768.

Jutzeler, M., White, J.D.L., Proussevitch, A.A., Gordee, S.M., 2016. Vesiculation and fragmentation history in a submarine scoria cone-forming eruption, an example from Nishiizu (Izu Peninsula, Japan). Bull. Volcanol. 78 (2), 7. http://dx.doi.org/10.1007/s00445-016-0999-2.

Kangro, K., Ansper-Toomsalu, A., Alikas, K., 2026. Spectral absorption characteristics and phytoplankton dynamics across optical water types: Evaluating Sentinel-2 and Sentinel-3 phytoplankton absorption retrieval accuracy in Boreal lakes. Remote. Sens. 15 (3), 1–24. http://dx.doi.org/10.3390/rs15030715.

Kano, K., 2003. Subaqueous pumice eruptions and their products: A review. Geophys. Monogr. Ser. 140, 213–229. http://dx.doi.org/10.1029/140GM14, ADS Bibcode: 2003GMS...140..213K, URL https://ui.adsabs.harvard.edu/abs/2003GMS...140..213K.

Klemas, V., 2010. Remote sensing techniques for studying coastal ecosystems: An overview. J. Coast. Res. 27 (1), 2–17. http://dx.doi.org/10.2112/JCOASTRES-D-10-00103.1.

Knaeps, E., Strackx, G., Meire, D., Sterckx, S., Mijnendonckx, J., et al., 2020. Hyperspectral reflectance of marine plastics in the VIS to SWIR. http://dx.doi.org/10.4121/12896312.v2, 4TU.ResearchData.

Kokaly, R.F., Clark, R.N., Swayze, G.A., Livo, K.E., Hoefen, T.M., Pearson, N.C., Wise, S.A., Benzel, W.M., Lowers, H.A., Driscoll, R.L., Klein, A.J., 2017. USGS Spectral Library Version 7. U.S. Geological Survey, Reston, VA, http://dx.doi.org/10.3133/ds1035.

Liu, Y., Wang, Y., Zhang, J., 2012. New Machine Learning Algorithm: Random Forest, vol. 7473, Springer, http://dx.doi.org/10.1007/978-3-642-34062-8_32, URL https://link.springer.com/chapter/10.1007/978-3-642-34062-8_32.

Mackey, D.J., O'Sullivan, J.E., Watson, R.J., 2002. Iron in the western Pacific: A riverine or hydrothermal source for iron in the equatorial undercurrent? Deep-Sea Res. I 49, 877–893.

Manga, M., Fauria, K.E., Lin, C., Mitchell, S.J., Jones, M.P., Conway, C.E., Degruyter, W., Hosseini, B., Carey, R., Cahalan, R., Houghton, B.F., White, J.D.L., Jutzeler, M., Soule, S.A., Tani, K., 2018. The pumice raft-forming 2012 Havre submarine eruption was effusive. Earth Planet. Sci. Lett. 489, 49–58. http://dx.doi.org/10.1016/j.epsl.2018.02.025, URL https://www.sciencedirect.com/science/article/pii/S0012821X18300876.

Mantas, V.M., Pereira, A.J.S.C., Morais, P.V., 2011. Plumes of discolored water of volcanic origin and possible implications for algal communities. The case of the Home Reef eruption of 2006 (Tonga, Southwest Pacific Ocean). Remote Sens. Environ. 115 (6), 1341–1352. http://dx.doi.org/10.1016/j.rse.2011.01.014, URL https://www.sciencedirect.com/science/article/pii/S0034425711000344.

Mitchell, S.J., Fauria, K.E., Houghton, B.F., Carey, R.J., 2021. Sink or float: Microtextural controls on the fate of pumice deposition during the 2012 submarine Havre eruption. Bull. Volcanol. 83, 80. http://dx.doi.org/10.1007/s00445-021-01497-6.

Ohno, Y., Iguchi, A., Ijima, M., et al., 2022. Coastal ecological impacts from pumice rafts. Sci. Rep. http://dx.doi.org/10.1038/s41598-022-14614-y.

Olgun, N., Duggen, S., Croot, P., Hoffman, L., 2008. Airborne volcanic ash trace metal release to the surface ocean and possible effects on marine primary production. In: Geophysical Research Abstracts, vol. 10, EGU2008–A–06029.

Pegler, S.S., Ferguson, D.J., 2021. Rapid heat discharge during deep-sea eruptions generates megaplumes and disperses tephra. Nat. Commun. 12, 2292. http://dx.doi.org/10.1038/s41467-021-22439-y.

Pistolesi, M., Aravena, A., Costantini, L., Vigiani, C., Cioni, R., Bonadonna, C., 2021. Explosive behavior of intermediate magmas: The example of cotopaxi volcano (Ecuador). Geochem. Geophys. Geosystems 22 (11), e2021GC009991. http://dx.doi.org/10.1029/2021GC009991, e2021GC009991 2021GC009991, arXiv:https://agupubs.onlinelibrary.wiley.com/doi/pdf/10.1029/2021GC009991, URL https://agupubs.onlinelibrary.wiley.com/doi/abs/10.1029/2021GC009991.

Pommerol, A., Schmitt, B., 2008. Strength of the H2O near-infrared absorption bands in hydrated minerals: Effects of particle size and correlation with albedo. J. Geophys. Res.: Planets 113 (E10), http://dx.doi.org/10.1029/2007JE003069, arXiv:https://agupubs.onlinelibrary.wiley.com/doi/pdf/10.1029/2007JE003069, URL https://agupubs.onlinelibrary.wiley.com/doi/abs/10.1029/2007JE003069.

Pope, E.L., Jutzeler, M., Cartigny, M.J.B., Shreeve, J., Talling, P.J., Wright, I.C., Wysoczanski, R.J., 2018. Origin of spectacular fields of submarine sediment waves around volcanic islands. Earth Planet. Sci. Lett. 493, 12–24. http://dx.doi.org/10.1016/j.epsl.2018.04.020.

Proud, S.R., et al., 2022. The January 2022 eruption of Hunga Tonga-Hunga Ha'apai volcano reached the mesosphere. Science 378, 554–557. http://dx.doi.org/10.1126/science.abo4076.

Redick, N.R., 2023. A review of pumice raft formation environments, saturation, and dispersal mechanisms. McGill Sci. Undergrad. Res. J. 18 (1), B19–B25. http://dx.doi.org/10.26443/msurj.v18i1.187, URL https://msurjonline.mcgill.ca/article/view/187.

Rosas-Chavoya, M., Gallardo-Salazar, J.L., López-Serrano, P.M., Alcántara-Concepción, P.C., León-Miranda, A.K., 2022. QGIS a constantly growing free and open-source geospatial software contributing to scientific development. Cuad. de Investigación Geográfica 48 (1), 197–213. http://dx.doi.org/10.18172/cig.5143, Number: 1, URL https://publicaciones.unirioja.es/ojs/index.php/cig/article/view/5143.

Schneider, C.A., Rasband, W.S., Eliceiri, K.W., 2012. NIH image to ImageJ: 25 years of image analysis. Nature Methods 9 (7), 671–675. http://dx.doi.org/10.1038/nmeth.2089, Publisher: Nature Publishing Group, URL https://www.nature.com/articles/nmeth.2089.

Siebert, L., Simkin, T., Kimberly, P., 2011. Volcanoes of the World: Third Edition. University of California Press, Google-Books-ID: 0DZrfpL9_DMC.

Spectra Vista Corporation, 2013. SVC HR-1024i User Manual, Revision 1.6. Spectra Vista Corporation, New York, NY, URL https://fsf.nerc.ac.uk/instruments/frfss/svc_hr1024i/.

Takeuchi, S., Ishige, K., Uesawa, S., Suwa, Y., 2024a. Unsinkable, long-drifting, millimeter-sized pumice of the 2021 eruption of Fukutoku-Oka-no-Ba submarine volcano. Prog. Earth Planet. Sci. 11 (1), 47.

Takeuchi, S., Ishige, K., Uesawa, S., Suwa, Y., 2024b. Unsinkable, long-drifting, millimeter-sized pumice of the 2021 eruption of Fukutoku-Oka-no-Ba submarine volcano. Prog. Earth Planet. Sci. 11 (1), 47. http://dx.doi.org/10.1186/s40645-024-00652-9.

Tome, C., 2021. Large amounts of fish are killed after swallowing pumice stones from undersea volcanic eruption, 14 Okinawan fisheries reeling from the damage as Okinawa and Japan coordinate on removal. Ryukyu Shimpo (English Edition), URL https://english.ryukyushimpo.jp/2021/10/29/34157/.

Upchurch, J., Schott, J., 2014. Worldview-3: New spectral capabilities. In: Proceedings of SPIE 9241, Earth Observing Systems XIX. http://dx.doi.org/10.1117/12.2063379.

Urai, M., 2014. Time series analysis of discolored seawater reflectance observed by advanced visible and near infrared radiometer type 2 (AVNIR-2) at Fukutoku-Okonaba submarine volcano, Japan. J. Volcanol. Geotherm. Res. 269, 23–27. http://dx.doi.org/10.1016/j.jvolgeores.2013.11.006, URL https://www.sciencedirect.com/science/article/pii/S0377027313003338.

Urai, M., Machida, S., 2005. Discolored seawater detection using ASTER reflectance products: A case study of Satsuma-Iwojima, Japan. Remote Sens. Environ. 99 (1), 95–104. http://dx.doi.org/10.1016/j.rse.2005.04.028, URL https://www.sciencedirect.com/science/article/pii/S0034425705001719.

Vermote, E., Wolfe, R., 2015. MOD09GQ MODIS/Terra Surface Reflectance Daily L2G Global 250 m SIN Grid V006. NASA EOSDIS Land Processes DAAC, http://dx.doi.org/10.5067/MODIS/MOD09GQ.006, Accessed 18 August 2025.

Vougioukalakis, G.E., Koutroulli, A., Sparks, S.R.J., Aspinall, W., Baxter, P.J., Bevilacqua, A., Francalanci, L., Kanellopoulos, C., Neri, A., Papazachos, C., Tadini, A., 2025. The kolumbo volcanic field, Greece: a review of evidence to reconstruct the 1650 CE eruption and to support hazard and risk assessment. Bull. Volcanol. 87, 55. http://dx.doi.org/10.1007/s00445-025-01824-1.

Wessel, P., Luis, J.F., Uieda, L., Scharroo, R., Wobbe, F., Smith, W.H.F., Tian, D., 2019. The generic mapping tools version 6. Geochem. Geophys. Geosystems 20 (11), 5556–5564. http://dx.doi.org/10.1029/2019GC008515, _eprint: https://onlinelibrary.wiley.com/doi/pdf/10.1029/2019GC008515, URL https://onlinelibrary.wiley.com/doi/abs/10.1029/2019GC008515.

Whiteside, A., Dupouy, C., Singh, A., Frouin, R., Menkes, C., Lefèvre, J., 2021. Automatic detection of optical signatures within and around floating Tonga-Fiji pumice rafts using MODIS, VIIRS, and OLCI satellite sensors. Remote. Sens. 13 (3), 501. http://dx.doi.org/10.3390/rs13030501, Number: 3 Publisher: Multidisciplinary Digital Publishing Institute, URL https://www.mdpi.com/2072-4292/13/3/501.

Whitham, A.G., Sparks, R.S.J., 1986. Pumice. Bull. Volcanol. 48 (4), 209–223. http://dx.doi.org/10.1007/BF01087675.

Wu, J., Cronin, S., Brenna, M., et al., 2025. Low sulfur emissions from 2022 Hunga eruption due to seawater–magma interactions. Nat. Geosci. 518–524. http://dx.doi.org/10.1038/s41561-025-01691-7.

Yeo, I.A., McIntosh, I.M., Bryan, S.E., Tani, K., Dunbabin, M., Dobson, K.J., Mitchell, S.J., Collins, P.C., Clare, M.A., Cathey, H., Duwai, I., Brandl, P.A., Stone, K., Manu, M.S., 2024. The 2019 pumice raft forming eruption of volcano-F (volcano 0403–091) and implications for hazards posed by submerged calderas. J. Volcanol. Geotherm. Res. 454, 108160. http://dx.doi.org/10.1016/j.jvolgeores.2024.108160, URL https://www.sciencedirect.com/science/article/pii/S0377027324001525.

Yoshida, K., Tamura, Y., Sato, T., Hanyu, T., Usui, Y., Chang, Q., Ono, S., 2022. Variety of the drift pumice clasts from the 2021 Fukutoku-Oka-no-Ba eruption, Japan. Isl. Arc 31 (1), e12441. http://dx.doi.org/10.1111/iar.12441, arXiv:https://onlinelibrary.wiley.com/doi/pdf/10.1111/iar.12441, URL https://onlinelibrary.wiley.com/doi/abs/10.1111/iar.12441.

Yoshida K., T.Y., 2022. Variety of the drift pumice clasts from the 2021 Fukutoku-Oka-no-Ba eruption, Japan - Yoshida - 2022 - island arc - Wiley online library. URL https://onlinelibrary.wiley.com/doi/full/10.1111/iar.12441.

Zheng, M., Mittal, T., Fauria, K.E., Subramaniam, A., Jutzeler, M., 2022. Pumice raft detection using machine-learning on multispectral satellite imagery. Front. Earth Sci. 10, 838532. http://dx.doi.org/10.3389/feart.2022.838532.